



# Altered solar wind-magnetosphere interaction at low Mach numbers: Coronal mass ejections

Benoit Lavraud, Joseph E. Borovsky

## ► To cite this version:

Benoit Lavraud, Joseph E. Borovsky. Altered solar wind-magnetosphere interaction at low Mach numbers: Coronal mass ejections. *Journal of Geophysical Research*, 2008, 113, pp.CiteID A00B08. 10.1029/2008JA013192 . hal-00377240

**HAL Id: hal-00377240**

**<https://hal.science/hal-00377240>**

Submitted on 21 Apr 2009

**HAL** is a multi-disciplinary open access archive for the deposit and dissemination of scientific research documents, whether they are published or not. The documents may come from teaching and research institutions in France or abroad, or from public or private research centers.

L'archive ouverte pluridisciplinaire **HAL**, est destinée au dépôt et à la diffusion de documents scientifiques de niveau recherche, publiés ou non, émanant des établissements d'enseignement et de recherche français ou étrangers, des laboratoires publics ou privés.

# Altered solar wind - magnetosphere interaction at low Mach numbers: coronal mass ejections

Benoit Lavraud<sup>1,2,3</sup> and Joseph E. Borovsky<sup>1</sup>

<sup>1</sup> Space Science and Applications, Los Alamos National Laboratory, Los Alamos, New Mexico, USA

<sup>2</sup> Centre d'Etude Spatiale des Rayonnements, Université de Toulouse (UPS), France

<sup>3</sup> Centre National de la Recherche Scientifique, UMR 5187, Toulouse, France

We illustrate some fundamental alterations of the solar wind – magnetosphere interaction that occur during low Mach number solar wind. We first show that low Mach number solar wind conditions are often characteristic of coronal mass ejections (CME), and magnetic clouds in particular. We then illustrate the pivotal role of the magnetosheath. This comes from the fact that low Mach number solar wind leads to the formation of a low thermal  $\beta$  magnetosheath downstream of the bow shock. This property influences magnetic forces and currents, in particular, and in turn alters magnetosheath – magnetosphere coupling. The implications of this unusual regime of interaction have generally been overlooked. Potentially affected phenomena include: (1) asymmetric magnetosheath flows (with substantial enhancements); (2) asymmetric magnetopause and magnetotail shapes; (3) changes in the development of the Kelvin-Helmholtz instability and giant spiral auroral features; (4) variations in the controlling factors of dayside magnetic reconnection; (5) cross polar cap potential saturation and Alfvén wings; and (6) global sawtooth oscillations. Here we examine these phenomena, primarily by use of global magneto-hydrodynamic simulations, and discuss the mechanisms that rule such an altered interaction. We emphasize the fact that all these effects tend to occur simultaneously so as to render the solar wind – magnetosphere interaction drastically different from the more typical high Mach number case. In addition to the more extensively studied inner magnetosphere and magnetotail processes, these effects may have important implications during CME-driven storms at Earth, as well as at other astronomical bodies such as Mercury.

## 1. Introduction

From both forecasting and basic physics viewpoints, there is a need for a better understanding of the solar wind – magnetosphere system during all types of solar wind conditions. Solar wind conditions change with time and the coupling with Earth's magnetosphere is thus also variable. We will show that the interaction of a low Mach number solar wind with the magnetosphere is drastically different from that for more typical high Mach numbers. Surprisingly, the effects of this type of solar wind are not often considered (although it constitutes a different regime of interaction) while it characterizes a number of geomagnetic storms driven by coronal mass ejections (CME).

Upstream of the Earth's magnetosphere, the solar wind is decelerated and diverted at the bow shock. The bow shock creates a hotter plasma region, the magnetosheath, which bathes the Earth's magnetosphere. The interaction between the solar wind and the magnetosphere is in fact mediated by the flowing magnetosheath. The coupling really occurs at the magnetopause, so that an accurate knowledge of the characteristics of the magnetosheath is crucial.

Early studies of the flows of the magnetosheath used a gasdynamic description [*Spreiter et al.*, 1966a; 1966b]. Although this is frequently adequate (i.e., at high solar wind Mach numbers), in reality the flow behavior is affected by magnetic fields. The magnetic forces that act on the flows become larger as the solar wind Mach number and

subsequent magnetosheath thermal  $\beta$  are lower [*Spreiter et al.*, 1966a; *Biernat et al.*, 2000], which tends to be the case for CMEs [*Gosling et al.*, 1987]. As previously shown by *Borovsky and Denton* [2006a], the lowest solar wind Mach numbers are typically associated with Magnetic Clouds (MC), a subset of CMEs.

In this paper, we list and describe a number of effects which, when combined, ought to render solar wind – magnetosphere coupling drastically different when the solar wind Mach number is low. The primary effects we discuss are: (1) asymmetric magnetosheath flows; (2) asymmetric magnetopause shapes; (3) changes in the development of the Kelvin-Helmholtz instability; (4) variations in the controlling factors of dayside magnetic reconnection; (5) cross polar cap potential saturation; and (6) global sawtooth oscillations. These effects, as well as an estimation of the evidence for them and our current understanding, are listed in Table 1 together with a few other secondary, expected effects. A brief introduction to each of the primary effects is made in the related sections (cf. Table 1). Our descriptions are primarily based on results from 3D global MHD simulations of the solar wind – magnetosphere interaction. We also illustrate their importance by use of relevant data analysis, although more detailed observational studies will be required in the future to fully explore these effects. The solar wind may have a low Mach number owing to low densities (e.g., on the day the solar wind almost disappeared [*Farrugia et al.*, 2000; 2008; *Le et al.*, 2000]), but here we mainly focus on low Mach numbers resulting from strong magnetic fields because such conditions are potentially conducive to intense geomagnetic storms. Section 2 describes the MHD model and data used for the study. The effects under consideration are described in section 3 and its subsections. A summary, and some insights on future works to be performed, are given in section 4.

## 2. Magneto-hydrodynamic model and data

We primarily employ global magneto-hydrodynamic (MHD) simulations of the solar wind – magnetosheath – magnetosphere system, using the facilities at the Community Coordinated Modeling Center (CCMC) at NASA Goddard Space Flight Center. We use the BATS-R-US model for the present study. Although we plan to compare various model results in the future, we expect that the basic conclusions of the present study would be similar with other models.

BATS-R-US is a global model of the solar wind – magnetosphere – ionosphere interaction. The model is based on the equations of ideal single-fluid MHD. These equations are solved on a three-dimensional structured grid, for which the cell size increases away from Earth. Numerical details, and example use of this code, may be found in, e.g., *Gombosi et al.* [2000] and references therein. The ionosphere is represented by a two-dimensional layer with prescribed finite Pederson and Hall conductivities. The magnetosphere-ionosphere coupling is performed as described in the work of *Ridley et al.* [2004].

In section 3.1 we use the hourly-averaged OMNI-2 solar wind dataset [King and Papitashvili, 2005], together with lists of intervals of coronal mass ejections [Cane and Richardson, 2003], magnetic clouds [e.g., Lepping *et al.*, 2006], high-speed streams, and global sawtooth oscillations. These latter two are combinations of lists compiled by R. L. McPherron, M. G. Henderson and the authors.

### 3. Implications of the low Mach number solar wind

In this paper we make use of many global MHD model runs for which we chose solar wind parameters as appropriate. It should be noted that runs are done with fixed solar wind conditions for about one hour, in order to reach a steady state, before results are used (there is one exception which is described in section 3.8). In this study we mainly tune the simulations according to the interplanetary magnetic field. It is possible that Mach number effects arising from varying the density and velocity (instead) would lead to somewhat different magnetosheath and magnetosphere properties (see Pulkkinen *et al.* [2007a] for some discussion of the latter). Also, the magnetosheath properties downstream of a quasi-parallel shock would be somewhat different from those for a perpendicular shock in the sub-solar region as used throughout this paper. Such considerations are beyond the scope of the present paper.

#### 3.1. Occurrence of low Mach number solar wind: Coronal Mass Ejections

In Figure 1, the normalized occurrence distribution (in %) of Alfvén Mach numbers from the OMNI (1-hour) dataset is binned for different sets of solar wind and magnetospheric conditions: (1) all solar wind conditions (black; median  $M_A = 7.5$ ), (2) coronal mass ejections (CME; orange; median  $M_A = 5.4$ ), (3) magnetic clouds (MC; red; median  $M_A = 3.9$ ), (4) high-speed streams (HSS; purple; median  $M_A = 8.0$ ) and (5) global sawtooth oscillation (SO; blue; median  $M_A = 4.4$ ) intervals. These intervals were taken from various sources (see section 2).

Figure 1 shows that low Alfvén Mach number intervals in the solar wind are primarily associated with CMEs, and in particular with the subset of MCs. The subset of MCs has been proposed to be CMEs crossed by the spacecraft in a central fashion, so that the magnetic flux rope structure is most easily identifiable (e.g., Jian *et al.* [2006] and references therein). In this framework, CMEs that are not classified as MCs correspond to non-central crossings of the same type of structures. Low Alfvén Mach number properties (high magnetic field and modest densities) can be expected as characteristic of the center of flux rope-type structures. Thus, that MCs statistically present lower Alfvén Mach numbers than the whole CMEs dataset, as observed in Figure 1, is compatible with this interpretation. CMEs have lower Alfvén Mach numbers than the typical solar wind and can even at times reach values close to or below one. Also, the most geoeffective CMEs, which tend to have large magnetic field magnitudes, are expected to have a lower average Mach

number than that for all CMEs displayed in Figure 1. All the effects, and their implications, of the interaction of the low Alfvén Mach number solar wind with the magnetosphere are thus critical during CME-driven storms. The implications for SOs are discussed later in section 3.8.

### 3.2. Resulting low- $\beta$ magnetosheath

Of interest to us is the fact that plasma properties in the magnetosheath, downstream of the bow shock, will be altered by the Mach number of the solar wind. Introducing the sonic and Alfvén speeds,  $V_s = (\gamma P/\rho)^{1/2}$  and  $V_A = (B^2/\rho\mu_0)^{1/2}$  respectively (with the plasma mass density  $\rho$ , thermal pressure  $P$ , magnetic field magnitude  $B$  and the ratio of specific heat  $\gamma$ ), in the perpendicular shock case the magnetosonic and Alfvén Mach numbers are (1)  $M_{MS} = V_{sw}/(V_s^2 + V_A^2)^{1/2}$  and (2)  $M_A = V_{sw}/V_A$ , respectively (where  $V_{sw}$  is the solar wind speed).

Figure 2a shows the Mach number dependence of the thermal  $\beta$  values downstream of a perpendicular shock from Rankine-Hugoniot [e.g., *Tidman and Krall*, 1971] jump conditions. For this calculation we used fairly low solar wind density and temperature, as is typical of magnetic clouds (see Figure caption for details). This figure shows that low Mach numbers lead to low  $\beta$  values in the downstream magnetosheath. For  $M_A \sim 2$  the downstream  $\beta$  value is lower by almost two orders of magnitude than for  $M_A \sim 20$ . For the parameters used in Figure 2, the downstream  $\beta$  value becomes lower than unity for  $M_A < 4$ . Figure 2a also shows that the  $M_{MS}$  and  $M_A$  are close to each other in the low Mach number regime. This comes from the fact that both Mach numbers primarily become low when  $V_A$  becomes high (low density and/or high magnetic field). In such a regime,  $V_A$  dominates over  $V_s$  and thus  $M_{MS}$  tends to get closer to  $M_A$ . Because  $M_{MS}$  is close to  $M_A$  (yet  $M_{MS} < M_A$  always) in the low Mach number regime, in the remainder of this paper we only use the Alfvén Mach number and simply refer to it as Mach number. Furthermore, that  $M_A$  and  $M_{MS}$  are close to each other is even truer during magnetic clouds since these are characterized by unusually low temperatures [*Gosling*, 1990], thus reducing the sonic speed  $V_s$ . Finally, Figure 2b shows the dependence of the shock compression ratio as a function of  $M_A$ . The shock compression ratio corresponds to the ratio of the downstream to upstream transverse magnetic fields. The well-known fact that the compression ratio lowers for lower Mach numbers is observed in Figure 2b. The two limiting values are a ratio of 4 at high Mach numbers (strong shock limit) and a ratio of 1 for  $M_A = 1$ , which in fact corresponds to the disappearance of the bow shock (sub-Alfvénic flow limit). The importance of the compression ratio will mainly be discussed in sections 3.6 and 3.7 later.

### 3.3. Asymmetric magnetosheath flows

A gasdynamic description will not result in magnetosheath flows that exceed the solar wind speed [*Spreiter et al.*, 1966a; 1966b]. Magnetosheath flows that exceeded that of the solar wind by 10 - 20 % have early been reported in the literature [*Howe and Binsack*, 1972; *Chen et al.*, 1993; *Petrinec et al.*, 1997]. Such observations were first interpreted in terms of enhanced magnetic tension of draped magnetic flux tubes that accelerate magnetosheath plasma along the magnetopause in the fashion of a magnetic “slingshot” [*Chen et al.*, 1993]. However, it was later argued [*Petrinec et al.*, 1997] (a) that such observations could result from either reconnection-related processes or high-energy particle leakage and (b) that magnetosheath flow may not exceed the solar wind speed by more than a few percent.

By contrast, *Lavraud et al.* [2007] and *Rosenqvist et al.* [2007] recently found magnetosheath flows that exceeded the solar wind flow speed by up to 60%, with peaks at  $\sim 1040$  and  $\sim 750$  km/s, respectively. Although these examples occurred for northward interplanetary magnetic field (IMF), the same acceleration mechanism may be expected to occur during southward IMF, i.e., during storm times, as will be addressed here as well.

Figure 3 shows equatorial two-dimensional (2D) cuts of the plasma speed from two global MHD simulations with solar wind Mach numbers (a)  $M_A = 14.90$  and (b)  $M_A = 1.99$  (see captions for detailed values). First, we note that the bow shock is farther from Earth as the solar wind Mach number is lower. As a result of an increase in downstream fast magnetosonic speed, the bow shock intuitively ought to retreat Sunward as the Mach number approaches 1, when it ultimately disappears [e.g., *Russell and Petrinec*, 1996]. Such distant bow shock locations have been observed during such low Mach number conditions [e.g., *Fairfield et al.*, 2001]. As a result the magnetosheath during low Mach number is much thicker.

During low Mach number (Figure 3b) we note the presence of large flows in the magnetosheath up to speeds of  $\sim 900$  km/s while the solar wind speed is only 650 km/s. Here we do not repeat but summarize the work by *Lavraud et al.* [2007], who demonstrated that these flows are outside the magnetopause, and just adjacent to it, since flow streamlines passing through them in the MHD simulation (e.g., Figure 3b) are not connected to Earth. The acceleration mechanism is not related to the occurrence of magnetic reconnection, but rather is the result of magnetic pressure gradient and tension forces along the flow streamline. Indeed, under low Mach number conditions, the low  $\beta$  of the magnetosheath (see section 3.2 and Figure 2) results in magnetic forces being dominant over the plasma pressure gradient force; this represents a strong deviation from the gasdynamic picture in which only plasma pressure gradient forces are considered. Under northward IMF conditions, solar wind magnetic field lines that cross the bow shock in the sub-solar region bend at the nose of the magnetopause. As the field lines eventually slide sideways along the magnetopause the dominant

magnetic forces lead to enhanced flow accelerations perpendicular to the magnetic field, in the equatorial plane. Based on the same MHD simulation as that shown in Figure 3b, *Lavraud et al.* [2007] further demonstrated the role of both magnetic pressure gradient and tension forces, being essentially of similar magnitude in the total flow acceleration. *Lavraud et al.* [2007] thus concluded that this acceleration is not a simple analogy to a magnetic slingshot effect, for which the magnetic tension force ought to dominate.

During the interval of large flow studied by *Lavraud et al.* [2007], the IMF was strongly northward with  $B_z = 15$  nT, the solar wind velocity was about 650 km/s, and both were steady. The solar wind density was first about  $1 \text{ cm}^{-3}$  (the conditions used for Figure 3b) but rose around the magnetopause crossing, so that the solar wind  $M_A$  was between 2.0 and 4.4 during the interval. Upon entering the magnetosheath, Cluster observed flows up to  $\sim 1040$  km/s. These flows were mainly perpendicular to the magnetic field and characterized by a thermal  $\beta$  much lower than unity. While such large plasma accelerations are often taken to be the signature of magnetic reconnection, two arguments demonstrated that this was not the case. First, the IMF was strongly northward so reconnection on the dayside magnetopause is not expected. Second, Cluster magnetic field, ion, and electron measurements unambiguously showed that Cluster was outside the magnetopause when the fast flows were detected (as detailed in *Lavraud et al.* [2007]). Those fast flows were thus detected in the magnetosheath itself, and just adjacent to the magnetopause (see also *Rosenqvist et al.* [2007]).

Figure 4 shows the dependence of the maximum flow speed found in the magnetosheath as a function of Mach number, as found from eight global MHD simulations with variable northward IMF strengths. This figure shows that magnetosheath flows are substantially enhanced as soon as the Mach number is lower than  $M_A = 6$ . In fact, the flows just adjacent to the magnetopause are even smaller than those shown in Figure 4 for the highest Mach numbers ( $M_A > 6$ ). Indeed, Figure 4 shows the largest flows in a region comprised between  $X = [-10, -50] R_E$  and  $Y = [-10, -30] R_E$ , and in the low Mach number regime (Figure 3b) the largest flows in this region are just adjacent to the magnetopause while in the high Mach number regime (Figure 3a) the largest flows are not along the magnetopause, but rather at some distance out in the magnetosheath. This means that the difference in the magnitude of the flows just adjacent to the magnetopause between low and high Mach numbers, which is relevant to the discussion of the Kelvin-Helmholtz instability discussed next in section 3.5, is even larger than that appearing in Figure 4. In addition, in their event study *Lavraud et al.* [2007] noted that the flows observed by Cluster were significantly larger than those predicted by the MHD simulations for the actual solar wind parameters. They suggested that dynamical and/or non-MHD effects may explain this difference, but it remains that in reality enhanced magnetosheath flows may be typically higher than in MHD simulations. This underestimation is likely also the result of limited grid resolution in the MHD simulations (cf. paragraph after next).

Figure 5 shows a 2D cut of the magnitude of the flows in the Y-Z plane at a distance  $X = -5 R_E$ , for a low Mach number ( $M_A = 1.99$ ) and an IMF oriented  $45^\circ$  from the pure northward direction (with over-plotted magnetosheath field lines for context). The influence of IMF orientation on the flow location is very clear. This figure highlights the fact that the acceleration resulting from enhanced magnetic forces only takes place perpendicular to the magnetic field, so that for purely northward IMF the enhanced flows are located in the equatorial region. But if the IMF rotates the flow location follows the IMF orientation.

The dependence of the flow channel structure for two different simulation grid resolutions is illustrated in Figure 6. It shows the flow speed profile at two different distances downtail ( $X = -4$  and  $-14 R_E$ ). The solid lines correspond to a spatial grid size as shown by the faint vertical dotted lines in the plot. The dashed curves show the speed profiles for a simulation grid of twice lower resolution. For the finest resolution, the enhanced flows are larger in magnitude and narrower in the Y direction compared to the lower resolution run. This Figure thus highlights the impact of grid resolution in terms of both flow magnitude and spatial extent. It is further noted that the magnetopause is quite diffuse (here it is simply the velocity gradient), thus showing that at such resolutions global MHD simulations are unable to form a thin magnetopause. This fact is, for instance, the main reason why the Kelvin-Helmholtz instability hardly develops in global MHD simulations, although such resolutions are already computationally expensive [Kuznetsova, private communication; see also section 3.5].

Figure 7 is meant to demonstrate that enhanced magnetosheath flows also occur under southward IMF conditions during low Mach numbers, i.e., during storm-time. Figure 7a is similar to Figure 3b (low  $M_A$  and northward IMF) but shows the X component of the velocity with over-plotted flow streamlines selected in the magnetosheath (red). Figures 7b and 7d also show equatorial cuts, respectively of the X component of the velocity and of the Z component of the magnetic field, but for a pure southward IMF orientation. These show similar magnetosheath streamlines to Figure 7a, plus one from the magnetotail (4'). The rough magnetopause position is illustrated in those plots with a white dashed line. While in the northward IMF case (Figure 7a) the magnetopause is easily identified as the inward boundary of the large flows, in the southward IMF case (Figures 7b and 7d) the magnetopause position has been found by use of the additional flow streamline (4'). Indeed, in Figure 7b streamline 2' is clearly a magnetosheath streamline originating in the solar wind. However, streamline 4', just adjacent to it, maps to the near-Earth reconnection line present in the simulation, which is identifiable by use of the Z component of the magnetic field (Figure 7d). The magnetopause is thus located in between streamlines 2' and 4' in the downtail region. On the dayside, the magnetopause is clearly identified from the change in sign of  $B_z$  (Figure 7d), but such an identification was not possible in the downtail region since  $B_z$  is southward, like in the magnetosheath, at locations anti-Sunward of the near-Earth reconnection line.



The flow speeds along two selected flow streamlines, for northward (1) and southward (1') IMF, are shown respectively as the black and red curves in Figure 7c. This figure shows that the acceleration mechanism leading to enhanced magnetosheath flows along the magnetopause also takes place during southward IMF, and with equivalent magnitude. From Figure 7b, it is noted that under southward IMF near-tail reconnection on the nightside leads to even stronger flows in the magnetotail itself than in the magnetosheath, but this is not further addressed here.

Flow streamlines (3) and (3'), respectively for northward (Figure 7a) and southward (Figure 7b) IMF, show the impact of reconnection on the dayside during the relevant IMF conditions for solar wind streamlines impinging upon the sub-solar magnetopause. Streamline (3), under northward IMF, ends up in the near-Earth tail after having been captured by double high-latitude reconnection on the dayside and convected along the dusk flank. Such a scenario under northward IMF has been previously shown to occur in MHD simulations [Ogino *et al.*, 1994; Fedder and Lyon, 1995; Raeder *et al.*, 1997; Song *et al.*, 1999; Li *et al.*, 2005; 2008], and has been suggested from observations [Onsager *et al.*, 2001; Øieroset *et al.*, 2005; Lavraud *et al.*, 2005; 2006]. Streamline (3') (Figure 7b) gets involved in sub-solar reconnection, as expected for southward IMF conditions. Although not shown here, the streamline in fact goes over the northern cusp and polar cap region at large Z distances, so that there is a projection effect. Finally, it is worth to mention that streamlines (2) and (2') do not get involved in the reconnection process on the dayside, while both (3) and (3') do. This means that the reconnection process, for both northward and southward IMF, only involves a limited part of the solar wind flow directed towards Earth, at least in these MHD simulations. This fact will be relevant in sections 3.6 and 3.7.

### 3.4. Asymmetric magnetopause and magnetotail shapes

Although early evidences and arguments for increased flattening of the tail with distance from Earth [Walters, 1964; Michel and Dessler, 1970; Formisano *et al.*, 1979; Sibeck *et al.*, 1986] and for dawn-dusk magnetopause asymmetries at geosynchronous orbit [Dmitriev *et al.*, 2004; Suvorova *et al.*, 2005] have been made, the magnetopause shape is often assumed to be axi-symmetric about the aberrated Sun-Earth line, i.e., so that the cross-section of the magnetosphere is circular. This assumption has been used in the most popular (semi-) empirical models of the magnetopause, e.g., by Sibeck *et al.* [1991], Petrinec and Russell [1996], Shue *et al.* [1997] and Kawano *et al.* [1999], although some more complex models have also been performed using Artificial Neural Network techniques [Dmitriev and Suvorova, 2000] or fits to asymmetric shapes from theoretical expectations [e.g., Zhuang *et al.*, 1981; Boardsen *et al.*, 2000] (see also Shue and Song [2002] for a review).

Figure 8 shows how the magnetopause shape changes with solar wind Mach number and IMF direction. For that purpose, the figure shows the current density magnitude (which maximum is believed to be located at or close to the magnetopause) from global MHD simulations, together with selected magnetic field lines for context. Figures 8a and 8b are Y-Z 2D cuts at  $X = -15 R_E$  for northward IMF and respectively for high (14.90) and low (1.99) Mach numbers. Figures 8c and 8d are for the same Mach numbers but for southward IMF, and the cuts are made at  $X = -5 R_E$ .

These figures highlight that the magnetopause is elongated along the IMF direction (cf. over-plotted magnetic field lines) for low Mach number conditions, while the magnetopause is more circular for high Mach numbers, as is usually assumed. In addition, comparison of Figure 8b and 8d shows that this elongation is most important during southward IMF. Under northward IMF and low Mach number, this elongation is mostly observable at some distance downtail, which is why we chose  $X = -15 R_E$  (Figure 8b) as opposed to  $X = -5 R_E$  for the southward IMF case (Figure 8d). The primary mechanism for this elongation of the magnetopause shape is essentially the same as for the strong flow acceleration: magnetic forces are increased and dominant in the low  $\beta$  magnetosheath and act to squeeze the magnetopause perpendicular to the magnetic field, i.e., on the flanks of the magnetosphere but not above the poles for purely northward or southward IMF (as in Figures 8b and 8d). That forces act perpendicular to the magnetic field implies that this asymmetric squeezing will follow the IMF orientation, as is the case for the magnetosheath flow acceleration process. This fact can be observed in Figure 9, where we show a 2D cut similar to Figure 8d (low Mach number), but for which the IMF clock angle was set at  $45^\circ$  from the pure southward direction (selected magnetic field lines are over-plotted for context).

That the elongation of the magnetopause is less pronounced for northward IMF may be explained by the impact of magnetic reconnection. It may stem from the occurrence of double high-latitude reconnection, during northward IMF, due to the action of reconnection being directed against the magnetosheath flow (the convection of reconnected field lines is Sunward and equatorward). This may act against the deformation of the magnetopause above the poles if it is possible to set a stable reconnection site there [cf. *Fuselier et al.*, 2000; *Avanov et al.*, 2001; *Lavraud et al.*, 2004]. By contrast, the occurrence of sub-solar reconnection during southward IMF does not act against the elongation. It may even allow further elongation as the plasma reconnected in the sub-solar region is strongly accelerated poleward towards the cusps and lobes.

Figures 3a and 3b show another interesting effect of low solar wind Mach numbers on the magnetopause shape. While for high Mach number and northward IMF the magnetotail is quite elongated in the downtail direction and goes beyond the region plotted in Figure 3a, under low Mach number the magnetotail appears substantially shorter (Figures 3b and 7a; see also *Song et al.* [1999]). In the MHD simulation results, this also results from the enhanced magnetic

forces that act to squeeze the magnetopause; this squeezing is more and more important as the magnetic field in the magnetotail decreases with downtail distance. Interestingly, Figures 7a and 7b show that this shorter magnetotail may not exist during southward IMF. This is likely related to the presence of a near-Earth reconnection line in the simulations (during such storm-time conditions) that may influence the pressure balance at the magnetopause by imposing large tailward flows in the magnetotail. Note, however, that the variability of the length of the magnetotail (1) needs to be confirmed by spacecraft observations, and (2) appears to be somewhat dependent upon the global MHD model used, but this is not further addressed here.

### 3.5. Onset location of the Kelvin-Helmholtz instability

As suggested and observed by *Chen et al.* [1993] (and more recently by *Rosenqvist et al.* [2007] and *Fairfield et al.* [2007]), the occurrence of fast flows in the magnetosheath just outside the magnetopause may influence the growth of large-scale waves on the magnetopause, through the velocity shear-dependent Kelvin-Helmholtz instability (KHI) [e.g., *Fujimoto and Terasawa*, 1994; *Wilber and Winglee*, 1995; *Otto and Fairfield*, 2000; *Nykyri and Otto*, 2001; *Matsumoto and Hoshino*, 2006]. Thus, it may in turn affect the transport of solar wind plasma into the magnetosphere [*Hasegawa et al.*, 2004; 2006] and the coupling of momentum from the solar wind into the magnetosphere [*Borovsky and Funsten*, 2003; *Rosenqvist et al.*, 2007].

Local, high-resolution simulations (MHD, hybrid, etc.) have been able to reproduce the KHI for flank magnetopause-type configurations (cf. references above). Such modeling has shown the occurrence of plasma transport associated with the instability, even in the MHD framework [*Nykyri and Otto*, 2001]. Unfortunately, global MHD simulations usually have too coarse resolution on the flanks to allow for the development of KHI waves, primarily owing to the magnetopause boundary being too thick [*Kuznetsova*, private communication, 2007]. The possible influence of the low Mach number solar wind on the onset location of KHI-driven vortices thus cannot be assessed directly from the present simulations. However, we may argue for such an influence according to the following.

Both the KHI threshold and its wave growth rate are functions of plasma parameters each side of the boundary [e.g., *Chandrasekhar*, 1961]. They are in particular functions of the velocity shear, the Alfvén velocities and the boundary thickness [e.g., *Walker*, 1981]. In the simplest configuration we may assume a thin boundary, equal magnetic fields each side of the boundary and a wave vector parallel to the shear-flow velocity. Note that under the low  $\beta$  magnetosheath conditions considered here, the magnetic field and plasma parameters are quite similar on each side of the boundary (in the equatorial plane for northward IMF), owing to the plasma pressure being low on both sides of the magnetopause. In this simplified configuration, it is found that the KHI threshold is reached for any finite velocity shear and that the wave

growth rate is proportional to the velocity shear magnitude [e.g., *Chandrasekhar*, 1961]. Although some studies have noted effects of the Mach numbers and plasma  $\beta$  [e.g., *Lai and Lyu*, 2006; *Matsumoto and Seki*, 2007] on the KHI development, it is still to be fully determined how departure from parallel fields or the three-dimensional nature of KHI vortices may tend to damp the KHI for low Mach number solar wind; in particular since the low  $\beta$  magnetosheath implies that magnetic forces will strongly act against any bending of the magnetic field. We do not investigate such possibilities further here. This is listed in section 4 as a future work to perform.

Figures 3 and 7c (see also Figure 3 of *Lavraud et al.* [2007]) show that while the magnetosheath speed along the magnetopause only reaches values close to that of the solar wind at a distance very far downtail for high Mach numbers, velocities close to that of the solar wind are reached as close as the dawn – dusk terminator for  $M_A \sim 2$ . Thus, despite the caution mentioned above, this suggests that the Kelvin-Helmholtz instability may grow faster under such conditions. It should be able to reach a non-linear stage (i.e., rolled-up vortices and plasma transport) faster and closer to the sub-solar region for low Mach numbers. From Figure 6, we note that magnetosheath flows adjacent to the magnetopause are significantly enhanced for  $M_A = 6$  and below.

There have been previous observational studies linking the presence of enhanced magnetosheath flows to the occurrence of KHI-driven waves. *Chen et al.* [1993] first noted that the presence of enhanced magnetosheath flows (10-20% above solar wind speed) likely was the driver of the observed waves on the magnetopause. *Fairfield et al.* [2007] recently came to the same conclusion for a similar type of event. Both the *Chen et al.* [1993] and the *Fairfield et al.* [2007] events occurred during strong northward IMF. *Lavraud et al.* [2007] reported magnetosheath flows of up to 1040 km/s (60% above the solar wind speed) just adjacent to the magnetopause. However, no signature of KHI waves was found, possibly owing to the dynamic nature of the magnetopause during the event. Recently, *Rosenqvist et al.* [2007] found large flows in the magnetosheath, up to  $\sim 750$  km/s (60% above solar wind as well). Interestingly, they related the presence of an unusual giant spiral arc in the polar cap region to the occurrence of KHI vortices driven by the enhanced magnetosheath flow.

That the occurrence of KHI-driven waves may depend upon the solar wind Mach number has not been investigated observationally to our knowledge. We thus wonder whether the occurrence of enhanced magnetosheath flows may lead to the instability growing faster during low Mach number, i.e., so that KHI-driven vortices may be statistically observed closer to the nose of the magnetosphere.

*Hasegawa et al.* [2006] recently showed that KHI waves that have reached a non-linear stage (i.e., rolled-up vortices) may be found from relatively simple spacecraft data analysis. Indeed, such rolled-up vortices have the singularity to lead to low-density regions with tailward speeds larger than that of the magnetosheath (i.e., rolled-up magnetospheric

plasma). Using the list of such rolled-up KHI vortices compiled by *Hasegawa et al.* [2006] on the basis of Geotail data, together with two more examples from the literature (a Cluster event by *Hasegawa et al.* [2004] and a Double Star event by *Taylor et al.* [2007]), we find that overall the events have Mach numbers that range about evenly between 3 and 13. This is shown in Figure 10a, which displays the Mach number during each event as a function of the  $X_{\text{GSM}}$  location of observation of the rolled-up vortices. We note, however, that only three events occurred sunward of  $X_{\text{GSM}} = -1 R_E$  and those correspond to solar wind  $M_A$  between 3.5 and 6.5. Although there appears a tendency for fully rolled-up vortices to be observed closer to the nose during low Mach number, the number of such events is at present too low to be conclusive.

Figure 10b shows the solar wind Mach number, as a function of the IMF clock angle, measured during giant spiral auroral features observed by the IMAGE spacecraft during great storms (i.e., minimum Dst < -250 nT) that occurred in the period 2000-2006. This list (courtesy of *J. Kozyra* [private communication]) is the only such list available presently. It shows that such auroral features tend to occur during low Mach number. It should be noted, however, that the fact that those events have been searched during great storms likely biases the outcome since large driving conditions are often associated with low Mach number, as we discuss in the next sections. As shown by Figure 10b, such spiral auroral features can be associated with northward, horizontal (although not during a great storm, the case of *Rosenqvist et al.* [2007] is also plotted in Figure 10b: it has a clock angle close to  $90^\circ$ ) and even southward IMF directions. Although KHI-driven waves have mostly been reported during northward IMF, it is possible that large magnetosheath flows and large-scale KHI-driven waves lead to such spiral auroral features during strong southward IMF. Large-scale KHI-driven waves have been found during large southward IMF conditions in global MHD simulations [*Kuznetsova*, private communication]. This possibility deserves further investigations, observationally in particular.

### 3.6 Factors controlling dayside reconnection

Global magnetospheric convection, which is further addressed in section 3.7 in relation to the cross polar cap potential (CPCP), is believed to be driven by dayside magnetic reconnection as a result of forcing by the solar wind. Determining the dayside reconnection rate from upstream solar wind conditions is however not so straightforward (e.g., CPCP saturation). For instance, the function that best couples indices of magnetospheric activity to solar wind conditions, to date, was recently found solely based on an empirical tuning procedure [e.g., *Newell et al.*, 2007]. To allow for more direct physical interpretations, *Borovsky* [2008] recently elaborated a complex coupling function. It relates solar wind properties to the dayside reconnection rate, based on first principles and parameterization from global magneto-hydrodynamic (MHD) simulations. This function constitutes the core of the present section.

Magnetic reconnection at the dayside magnetopause is central to solar wind – magnetosphere coupling. When theories of this coupling are constructed the solar wind electric field is traditionally taken as a starting point [Gonzalez and Mozer, 1974; Siscoe and Crooker, 1974; Burton *et al.*, 1975; Perrault and Akasofu, 1978; Kan and Lee, 1979; Lei *et al.*, 1981; Wygant *et al.*, 1983; Gonzalez and Gonzalez, 1984]. Indeed, it is typically believed that the solar wind electric field “drives” dayside reconnection [e.g., Siscoe and Crooker, 1974; Wygant *et al.*, 1983; Goertz *et al.*, 1993; Freeman and Farrugia, 1999], i.e., that the solar wind electric field sets the electric field at the magnetopause and thus the dayside reconnection rate [Sonnerup, 1979; Vasyliunas, 1984; Schindler *et al.*, 1988].

But magnetic reconnection is a local process. When two identical plasmas reconnect, the reconnection rate is governed by the local Alfvén speed in the plasma near the reconnection site [Parker, 1973; Birn *et al.*, 2001]. When two plasmas that are not identical reconnect (such as the magnetosphere and magnetosheath), the question recently arose as to what exact factors control the reconnection rate [Borovsky and Steinberg, 2006; Borovsky and Denton, 2006a]. Two-dimensional [Borovsky and Hesse, 2007; Birn *et al.*, 2007] and three-dimensional [Borovsky *et al.*, 2008a] MHD simulations were performed to determine the parameters that control such asymmetric magnetic reconnection. To study dayside reconnection rates in global MHD simulations, Borovsky *et al.* [2008a] utilized a high resolution grid at the dayside magnetopause ( $1/16 R_E$ ) together with a localized “spot” of resistivity along the magnetopause in the equatorial plane, and all the way towards dawn and dusk. The logic behind this is (a) to force magnetic reconnection to be in a fast regime, which is believed to be the case for the magnetosphere and (b) to prevent numerical errors from controlling the reconnection rate. The reader is referred to Borovsky *et al.* [2008a] for further details. As for the above reference, this places the present results and discussions in the hypothesis of fast magnetic reconnection; that is, with a supposedly constant dimensionless reconnection rate ( $\sim 0.1$ ) but a variable rate of magnetic flux reconnection (i.e., the electric field), although observations have revealed probable deviations from this assumption [e.g., Fuselier *et al.*, 2005; Rosenqvist *et al.*, 2008].

The “special” simulations of Borovsky *et al.* [2008] confirmed that reconnection is a local process, so that its rate is governed by meso-scale plasma parameters near the reconnection site. For the magnetosphere that means that the solar wind electric field, in particular, does not directly drive dayside magnetic reconnection. Together with other solar wind, magnetosheath and magnetosphere properties it determines the parameters near the reconnection region, which in turn control the reconnection rate. For instance, as discussed later, this depends on the shock properties and on the geometry involved, i.e., how the plasmas and fields flow near and around the region that will undergo reconnection, and these properties are Mach number-dependent.

Theory and simulations show that four parameters govern the reconnection rate for non-identical plasmas: the magnetic field strengths and the mass densities on each side of the reconnection site [Cassak and Shay, 2007; see also Swisdak and Drake, 2007]. These four parameters form a hybrid Alfvén speed which controls the rate. Applying the Cassak-Shay formula to dayside reconnection, with  $B$  for magnetic field,  $\rho$  for plasma density and the subscript “s” for magnetosheath and “m” for magnetosphere, the dayside reconnection rate  $R$  is:

$$R = 2 K (B_m B_s)^{3/2} (\rho_m B_s + \rho_s B_m)^{-1/2} (B_m + B_s)^{-1/2} . \quad (1)$$

$K \approx 0.1$  is a coefficient representing the geometry of the inflow and outflow at the reconnection site, i.e., the dimensionless reconnection rate [cf. Borovsky, 2008]. Note that the mass density of the magnetospheric plasma enters into the reconnection rate: hence it can exert some control over solar wind – magnetosphere coupling, as recently evidenced by Borovsky and Denton [2006b] during times of dayside plasmaspheric drainage plumes.

From first principles and fits to special global MHD simulation results (like the one used in Borovsky *et al.* [2008a]), Borovsky [2008] further derived a formula that expresses the dayside reconnection rate in terms of upstream solar wind parameters. Again, the idea is that dayside reconnection rate is governed by local plasma properties and that whatever controls those properties controls reconnection. The starting point was the Cassak-Shay formula applied to the dayside reconnection site (expression (1)). Using the Rankine-Hugoniot relations at the bow shock and some knowledge about the properties of the magnetosheath behavior (by use of parameterization from global MHD simulations), three of these four parameters ( $B_m$ ,  $B_s$ , and  $\rho_s$ ) were expressed in terms of upstream solar wind parameters. These expressions were then inserted into the Cassak-Shay formula to obtain a “solar wind control function”, i.e., a reconnection rate written in terms of upstream solar wind parameters:

$$R = K' \sin(\theta/2) \rho v^2 (1 + 0.5 M_{ms}^{-2}) (1 + \beta_s)^{-1/2} [C \rho + (1 + \beta_s)^{-1/2} \rho_m]^{-1/2} [(1 + \beta_s)^{1/2} + 1]^{-1/2} \quad (2)$$

where

$$\beta_s = 3.2 \times 10^{-2} M_A^{1.92}$$

is the plasma  $\beta$  of the magnetosheath near the nose of the magnetosphere,

$$C = \{ [1/4]^6 + [1/(1 + 1.38 \log_e(M_A))]^6 \}^{-1/6}$$

is the compression ratio of the bow shock,

$$M_{ms} = v / ((B/4\pi\rho) + 2P/\rho)^{1/2}$$

is the magnetosonic Mach number of the solar wind, and

$$M_A = v (4\pi\rho)^{1/2} / B$$

is the Alfvén Mach number of the solar wind.  $K'$  is a constant that derives from  $K$  as defined for expression (1) above [cf. Borovsky, 2008]. A term  $\sin(\theta/2)$  was also added to account for component reconnection when the IMF has a clock

angle of  $\theta$ . In these expressions  $v$ ,  $\rho$ ,  $B$ , and  $P$  are the speed, mass density, magnetic field strength, and particle pressure (thermal plus kinetic) in the upstream solar wind. As can be seen from expression (2), the control function is nonlinear, strongly Mach number-dependent, and does not resemble any standard driver functions in the literature. The control function was not derived using a “tuning” procedure and it has no explicit free parameters.

The physical interpretation of the control function (expression (2); see also *Borovsky* [2008]) is that solar wind pressure  $\rho v^2(1+0.5M_{ms}^{-2})$  (the reader is reminded that, in first approximation,  $\rho v^2(1+0.5M_{ms}^{-2}) = \rho v^2 + B^2/8\pi + P_{th}$  is the total pressure of the solar wind) largely controls the reconnection rate, essentially by setting the strength of the magnetic field at the nose of the magnetosphere via pressure balance. In the low Mach number regime, the compression ratio  $C \approx 1 + 1.38\log_e(M_A)$  and the magnetosheath  $\beta_s \ll 1$ . Using these, expression (2) simplifies to:

$$R = 2 K' \sin(\theta/2) \rho v^2 (1+0.5M_{ms}^{-2}) [\rho(1 + 1.38\log_e(M_A)) + \rho_m]^{-1/2} \quad (3)$$

For  $\rho_m \ll \rho(1+1.4\log_e(M_A))$  (low density magnetosphere), which is often the case, expression (3) for the low Mach number limit becomes:

$$R = 2 K' \sin(\theta/2) \rho^{1/2} v^2 (1+0.5M_{ms}^{-2}) / (1 + 1.38\log_e(M_A)) \quad (4)$$

Expression (4) is significantly different from the high Mach number limit of expression (2), which is:

$$R = K' \sin(\theta/2) \rho v^2 \beta_s^{-3/4} [4\rho + \beta_s^{-1/2}\rho_m]^{-1/2} \quad (5)$$

For  $\rho_m \ll \rho(1 + 1.4 \log_e(M_A))$  (low density magnetosphere) expression (5) for the high Mach number limit further reduces to:

$$R = 3.28 \sin(\theta/2) n^{-0.22} v^{0.56} B^{1.44} \quad (6)$$

where  $R$  is in gauss.km/s,  $v$  is in km/s,  $B$  is in nT, and  $n$  is in  $\text{cm}^{-3}$ .

In Figure 11, we use expression (2) to explore the variation of the dayside reconnection rate as a function of solar wind Mach number (always Alfvén Mach number from now on). This is a parametric study of Eq. (2): the parameters ranges are not necessarily realistic, in particular at high Mach numbers. In panel (a) the variation in the Mach number is obtained by varying only the magnetic field strength of the solar wind, in panel (b) the variation is obtained by varying only the density, and in panel (c) the variation is obtained by varying only the solar wind speed. The reconnection rate  $R$  (left axis) is plotted as the black curves and the low Mach number and high Mach number asymptotic expressions (3) and (5) are plotted as the black dashed curves. In each panel, the solar wind parameter that was varied is plotted in green (right axis) and the values used for all other parameters are given. Values of the reconnection rate scaled by use of the parameter  $Q$  [*Siscoe et al.*, 2002a; 2004] are also given (red curves). This parameter is related to the occurrence of cross polar cap potential saturation; these curves are thus discussed in section 3.7 next.



In Figure 11a, the solar wind density and speed are held constant so that  $M_A \propto B^{-1}$ . Although not discussed in details here, there are subtleties in the behavior of the curve (its gradients in particular) that depend on which of the terms composing the function is dominant, as a function of Mach number. However, on average the behavior is so that an increase in solar wind magnetic field, for all other parameters held constant, leads to an increase in dayside reconnection rate. This is essentially due to an increased solar wind magnetic field always leading to an increased magnetic field near the nose of the magnetopause.

In Figure 11b, the solar wind density is varied, but other parameters are held constant: in this case  $M_A \propto n^{1/2}$ . In the low Mach number regime the reconnection rate increases with increasing Mach number. This is simply understood as the reconnection rate varying as the solar wind dynamic pressure divided by the square root of the solar wind density (expression (4)). This gives  $R \propto n^{1/2}v^2$ , and since  $n \propto M_A^2$  and the velocity is constant, this gives  $R \propto M_A^1$ . At high Mach numbers, the increasingly high  $\beta$  of the magnetosheath implies a decrease of the magnetic field in the magnetosheath. This overcomes the increasing solar wind pressure effect so as to cause the reconnection rate  $R$  to decrease with increasing  $M_A$  (if varied according to density).

In Figure 11c, the solar wind speed is varied to produce the variation in Mach number: in this case  $M_A \propto v^1$ . The reconnection rate at the dayside magnetopause increases for increasing solar wind speed (or Mach number) for all regimes of Mach number. As for the case of Figure 11a, we do not discuss all the subtleties of this curve, but essentially here an increase in velocity leads to an increase in dynamic pressure which effect is to always increase the magnetic fields near the magnetopause from pressure balance consideration. In the high Mach number regime, there is no decrease in reconnection rate like that observed when varying the density because the dynamic pressure depends on the square of the velocity, while it is only linear with density. Expression (6) depicts this behavior with a negative exponent to the density while a positive one for the velocity.

The “density” effect captured in Figure 11b, with an increase in reconnection rate for increasing density at low Mach numbers while a decrease at high Mach numbers, represents an effect previously reported by *Lopez et al.* [2004] (see also *Kataoka et al.* [2005]). *Lopez et al.* [2004] observed that, unlike previous studies which suggest that solar wind density variations have little effect on solar wind – magnetosphere coupling, the low Mach number MHD simulations they ran led to an increase in coupling (increased magnetospheric currents) for increasing solar wind density. Their explanation is that, if starting from a low Mach number solar wind for which the compression ratio at the bow shock is considerably less than 4, an increase in density increases the Mach number and shock compression ratio, thus resulting

in a stronger magnetosheath magnetic field even if the solar wind magnetic field and velocity are held constant. This stronger magnetic field applied to the magnetopause is deemed to increase the reconnection rate.

We note that the solar wind electric field ( $vB_z$ ) is assumed to be the driver by *Lopez et al.* [2004]. If that were the case then one may argue that since the velocity decreases at the bow shock as much as the transverse magnetic field increases, the electric field ( $vB_z$ ) behind the shock should not differ even in the low Mach number limit. An analysis using the driver function given by expression (2) indicates that the increase in magnetosheath magnetic field is only part of the story: at the same time the magnetosheath density and the magnetospheric magnetic field also increase. For the parameters of the MHD simulation of *Lopez et al.* [2004], the reconnection rate as a function of the solar wind density is plotted in Figure 12a. In Figure 12b the four plasma parameters that control the dayside reconnection rate ( $B_m$ ,  $B_s$ ,  $n_m$ , and  $n_s$ ) are plotted, together with the shock compression ratio  $C$ . As the solar wind density increases, the solar wind dynamic pressure increases and causes the magnetospheric magnetic field ( $B_m$ ) to increase by pressure balance with the solar wind. Similarly, the magnetosheath magnetic field near the nose ( $B_s$ ) increases by pressure balance. At low Mach numbers where the magnetosheath  $\beta$  is low, pressure balance is such that  $B_s \approx B_m$ , but at high Mach numbers  $B_s < B_m$  because plasma pressure in the high  $\beta$  magnetosheath enters the pressure balance significantly. According to the Cassak-Shay formula (expression (1)), the increases in  $B_m$  and  $B_s$  both act to increase the reconnection rate, while an increase in solar wind density in the denominator of the Cassak-Shay formula acts to decrease the rate. At low mach numbers the effects from the magnetic field increases beat the effect from the density increase and so the net reconnection rate increases. At high Mach numbers, the solar wind density effect dominates (owing to a large magnetosheath  $\beta$ ) and the net reconnection rate decreases with increasing solar wind density. Also, this decrease in reconnection rate for increasing densities at high Mach numbers (Figures 11b and 12a) appears consistent with the observational results of *Scurry and Russell* [1991], where they suggest that solar wind – magnetosphere coupling efficiency diminishes at large Mach numbers owing to a lowering of the reconnection rate.

### 3.7. Cross polar cap potential saturation

It is now a consensus (see *Shepherd* [2007] for a recent review) that during strong solar wind driving the cross polar cap potential (CPCP) tends to saturate: saturation means that the observed CPCP (as measured from ground instruments or low altitude satellites) is less than one would expect for a given strength of the solar wind driver, i.e., usually assumed to be the solar wind electric field [e.g., *Reiff et al.*, 1981; *Wygant et al.*, 1983; *Reiff and Luhmann*, 1986; *Ober et al.*, 2003; *Hairston et al.*, 2005]. This saturation also shows up in a number of geomagnetic indices [e.g., *Weimer et al.*, 1990; *Nagatsuma*, 2004; *Borovsky and Denton*, 2006a].

A number of physical explanations have been suggested in the literature [*Shepherd, 2007*]. These are related to: (1) a lowering of the subsolar reconnection rate due to a decreased magnetic field near the dayside magnetopause [*Hill et al., 1976*]; (2) a related argument due to the limitation of the Region 1 current system strength [*Siscoe et al., 2002a; 2002b; 2004*]; (3) a shortening of the dayside reconnection X-line limiting the integrated value of the reconnection electric field [e.g., *Pudovkin et al., 1985; Raeder and Lu, 2005; Ridley, 2005*]; (4) the possibility that ionospheric convection saturates but not magnetospheric convection, i.e., in the presence of a field-aligned potential [*Russell et al., 2001*]; (5) a blunter magnetosphere with geometrical (and magnetosheath flow) considerations suggesting a lower dayside reconnection rate [*Merkine et al., 2003*]; (6) a decrease in convection by mass loading from ionospheric outflows [*Winglee et al., 2002*], and (7) a saturation mechanism based on a circuit analog of a generator-load system [*Ridley, 2007; Kivelson and Ridley, 2008*]. In addition, it is well accepted that higher ionospheric conductivity increases the saturation level [e.g., *Hill et al., 1976; Siscoe et al., 2002b; Ober et al., 2003*]. Here we discuss global MHD simulation results in comparison with some of the models listed above and show how saturation relates to low Mach number solar wind, in the case of Earth in particular.

According to eq. (1) of *Siscoe et al. [2004]*, a simple parameter predicts when the CPCP will be saturated, and by how much. The amount of saturation can be expressed as  $(1+Q)^{-1}$  where  $Q$  is a dimensionless parameter defined as:

$$Q = \Sigma_p V_A / 806 \quad (7)$$

Substantial saturation occurs when  $Q$  exceeds about 2, wherein the CPCP is only 33% of its expected value. In expression (7)  $\Sigma_p$  is the height-integrated Pedersen conductivity of the ionosphere (in Siemens) and  $V_A$  is the Alfvén speed of the solar wind upstream of the bow shock (in km/s). As noted by *Ober et al. [2003]*, the ionospheric conductivity  $\Sigma_p$  can be expressed as  $\Sigma_p = 0.77 F_{10.7}^{1/2}$ , where  $F_{10.7}$  is the 10.7-cm radio flux from the sun, which is a proxy for the solar UV flux. Using this, expression (7) is rewritten in the simple form:

$$Q = V_A F_{10.7}^{1/2} / 1050 \quad (8)$$

Note that *Borovsky and Denton [2006a]* expressed  $Q$  in terms of  $V_A$  and  $S_N$ , where  $S_N$  is the monthly averaged sunspot number, which is also a proxy for the solar UV flux. However, the UV flux of the Sun varies considerably within a month and expressing  $Q$  in terms of  $S_N$  can thus be quite inaccurate [*Denton, private communication, 2007*]. The use of a dependence on  $F_{10.7}$ , which is available at one-day resolution from the National Geophysical Data Center, is thus preferred here. In a similar fashion to *Borovsky and Denton [2006a]*, for each list of solar wind structures defined previously in section 2 (also used in Figure 1) we plot the occurrence distribution of the saturation parameter  $Q$  in Figure 13. As can be seen, the  $Q$  value tends to be unusually high for coronal mass ejections (CMEs) and the subset of magnetic clouds (MC), in particular: these structures are the most likely drivers of CPCP saturation. This is simply

consistent with the fact that CMEs have high Alfvén speeds which lead to large  $Q$  values (high Alfvén speed corresponds to low Mach number). The limited range of variation of  $F_{10.7}$  (from  $\sim 10$  to  $300 \text{ } 10^{22} \text{ J.s}^{-1} \text{ m}^{-2} \text{ Hz}^{-1}$ ) and the fact that  $Q$  depends on the square root of  $F_{10.7}$  make the Mach number (Alfvén speed) the principal factor leading to CPCP saturation at Earth. In the following we will illustrate why the solar wind Mach number plays an important role in this context.

There are several explanations as to why the CPCP saturates (see above). Here we only address the possibility of (1) a shortening of the dayside reconnection X-line, (2) a reduction of dayside reconnection rate owing to changes in the magnetosheath flow pattern or to (3) increased region 1 currents, and (4) a generator-load coupling effect. In the latter the MHD dynamo generated poleward of the cusp on reconnected magnetic field lines (i.e., subsequent to dayside reconnection) is shorted out by the high conductivity of the ionosphere, i.e., resulting in a voltage decrease in the coupled generator-load system [Ridley, 2007; Kivelson and Ridley, 2008]. Note that generator-load saturations are familiar concepts in other fields of space physics [e.g., Drell *et al.*, 1965; Scholer, 1970; Neubauer, 1980].

Figure 14 illustrates CPCP saturation as observed in global MHD simulations. Although it is not known whether the actual CPCP saturation process can be accurately described by such simulations, that saturation does occur in MHD simulations of the magnetosphere-ionosphere system may be taken as an indication that the process happening there may be the real one. However, measurements would ultimately have to demonstrate this. Figure 14 shows CPCP values obtained from various simulations using parameters similar to those utilized previously (section 3.3 and 3.4), with a density of  $1 \text{ cm}^{-3}$  and a velocity of 650 km/s while varying the (purely southward) magnetic field strength (solid curve), and by varying the density from 1 to  $12 \text{ cm}^{-3}$  for a constant electric field with  $B_z = -15 \text{ nT}$  (as the large points arranged vertically in the plot). For context, we also show the CPCP estimation from the Hill-Siscoe formula [Siscoe *et al.*, 2002a] as the dashed curve and from a straight integration of the solar wind electric field (in the same fashion as done by Ridley [2007]) as a dotted line, assuming an effective magnetosphere radius of  $20 R_E$ . The latter is meant to give an estimate of how the CPCP would behave if there were no saturation, i.e., if the CPCP scaled linearly with the solar wind electric field. Both are estimated using the parameters from the MHD results of the solid line. The authors are unsure about the origin of the difference between the Hill-Siscoe estimation and the MHD results in Figure 14 (dashed and solid lines, respectively). However, we are mainly interested in a qualitative understanding of CPCP saturation and do not address this issue any further here.

The solid curve in Figure 14 highlights the fact that CPCP saturation does occur in global MHD simulation. We may therefore analyze these results to obtain clues as to what may be the fundamental mechanisms behind this effect. First, Figure 14 shows that CPCP saturation is related to the solar wind Mach number. This is observed in the fact that when

the solar wind density is varied (large data points in Figure 14), for the same solar wind electric field, the lowest CPCP corresponds to a low Mach number ( $M_A = 1.99$  and  $N_{SW} = 1 \text{ cm}^{-3}$ ) while a higher CPCP is obtained for larger Mach numbers (e.g.,  $M_A = 6.88$  and  $N_{SW} = 12 \text{ cm}^{-3}$ ). Also, while for an increased solar wind density the reconnection X-line extent must decrease due to a shrinkage of the whole magnetosphere (from pressure balance consideration), the CPCP actually increases. This is shown by the same set of simulations (large data points in Figure 14), for which the lowest CPCP corresponds to a low solar wind density ( $1 \text{ cm}^{-3}$ ) while a higher CPCP is obtained for larger density ( $12 \text{ cm}^{-3}$ ). This demonstrates that, although the extent of the reconnection X-line is an important factor that needs to be taken into account (as has been done by *Siscoe et al.* [2002a] or *Ridley* [2005] for instance), the shortening of the reconnection X-line may not be the fundamental process leading to CPCP saturation. That the CPCP increases for increasing density results here from the density effect described in the previous section 3.6, i.e., from an increase in dayside reconnection rate and occurs because the Mach number increases.

In their work, *Merkine et al.* [2003] (see also *Merkin et al.* [2005]) primarily studied the process of CPCP saturation from global MHD simulations by varying the ionospheric conductance. They found that saturation occurs due to a bulging of the magnetospheric lobes which alters both the reconnection rate and the flows in the magnetosheath. From the simulations performed for this paper, by varying the Mach number but keeping the ionospheric conductance constant, we find that the magnetosheath flow pattern is significantly altered at low Mach numbers. The result is that the amount of solar wind magnetic flux that eventually gets involved in the reconnection process at the magnetopause is typically smaller at low Mach number: the flow of the magnetosheath appears to divert more around the obstacle. In other words, the effective extent of solar wind that interacts with the magnetosphere at the magnetopause is smaller. The total potential available, which follows magnetosheath flow streamlines and then maps along the reconnection X-line, is thus smaller. Although our first analyses highlight this as an important reason for CPCP saturation, further analyses of the magnetosheath flows in those simulations revealed that numerical effects can alter this mechanism depending on (1) the simulation grid size, (2) the numerical scheme used, and (3) the resistivity model used near the reconnection site (i.e., runs with only numerical resistivity and others with prescribed finite resistivity, as used next for instance). Thus, although it appears that the nature of magnetosheath flow is important for CPCP saturation, and that these are significantly altered at low Mach number, we postpone such detailed analysis owing to possible numerical issues.

The reconnection X-line length, the dayside reconnection rate and the magnetosheath flow patterns are likely all important parameters which add-up in determining the CPCP potential. They have to represent the amount of solar wind potential that is available, i.e., the undisturbed generator voltage into which the magnetosphere can tap. But there may be other processes that add to the CPCP saturation.

For the purpose of investigating the influence of the region 1 currents on reconnection rate at the dayside magnetopause during CPCP saturation (i.e., the *Hill et al.* [1976] interpretation) we made use of a special global MHD run (with a high grid resolution and a localized “spot” of resistivity along the magnetopause as explained in section 3.6 and *Borovsky et al.* [2008a]). The ionospheric conductance is first held constant at 5 S but is ramped up to 20 S in the middle of the run, as shown in Figure 15b. The resulting CPCP from the MHD simulations is shown in Figure 15a. The CPCP substantially saturates when the ionospheric conductance is increased, as expected. Using the same MHD simulation, Figure 16 shows cuts of the magnetic field profile along the Sun-Earth line on the dayside, in red for low conductance and in blue for high conductance. For context, a pure dipole magnetic field profile is shown with a dashed grey curve. This Figure demonstrates that the magnetic field magnitude in the dayside magnetosphere is significantly reduced for high conductivity. This results from the negative feedback (magnetic perturbation) of increased region 1 currents during saturation and is consistent with the expectations of the Hill model. However, the magnetic field magnitude just inside of the magnetopause, close to the reconnection region, is very similar for both conductances. Only the location of the magnetopause is different, being closer to Earth for a larger conductance. This simply stems from pressure balance considerations, where the globally decreased field in the magnetosphere leads to an equilibrium magnetopause closer to Earth: but the field strength at the equilibrium point is essentially the same. This need for equilibrium at the dayside magnetopause, leading to a negligible change in the magnetic field strength there in the saturation regime, was previously noted by *Siscoe et al.* [2002b].

The reconnection rate at the dayside magnetopause is a function of the local parameters near the reconnection site, as discussed in the previous section 3.6. Since the field strengths are the same, the reconnection rate does not significantly change between the two conductivity cases. This is shown by the light blue and magenta curves of the resistive electric field ( $\eta J_V$ ) in Figure 16, which represent the merging electric field in the reconnection region (where a finite resistivity is applied). Therefore, at least for these runs, one may conclude that region 1 currents lower the magnetic field in the dayside magnetosphere but they do not lower the magnetic field near the reconnection site, contrary to the Hill model expectations. Pressure balance considerations lead to a magnetopause closer to Earth but the reconnection rate there is not altered. On the other hand, that the reconnection rate is not altered appears incompatible with the fact that the CPCP potential is lower in the high conductivity case. Consideration of the distribution of the reconnection rate along the magnetopause, of the X-line length and of the magnetosheath flows may be able to explain this. As stated previously, some numerical issues prevent us from pursuing this type of complex analyses from the present simulations results.

We finally discuss the interpretation of CPCP saturation given by *Ridley* [2005; 2007] and *Kivelson and Ridley* [2008] in comparison to that of *Siscoe et al.* [2002; 2004]. Although their formulations are derived differently (eq. (1) of

*Siscoe et al.* [2004] and eq. (7) of *Kivelson and Ridley* [2008]), they yield similar expressions for CPCP saturation occurrence and magnitude: both can be expressed with a  $(1+Q)$  factor in the denominator, e.g., expression (7) (from the Hill-Siscoe model). While Hill-Siscoe interpret CPCP saturation as the result of increased region 1 currents and a lowering of dayside reconnection rate, the interpretation of *Kivelson and Ridley* [2008] involves the effects of a coupled generator-load system. In the latter explanation, the presence of a solar wind Alfvén speed in the  $Q$  factor comes from the fact that the maximum current that the generator can deliver is limited by the Alfvén conductance of the source solar wind. At the other end of the circuit, the current required to flow in the load (the ionosphere) to maintain the potential across it depends upon the conductance of the load. The coupling of this system leads to a saturation of the potential whenever the load tries to draw too much current (by increasing its conductance) and/or when the generator becomes unable to supply enough current (by increasing the solar wind Alfvén speed) to maintain the potential across the load. An analysis of the *Kivelson and Ridley* [2008] model arrives at an expression for  $Q$  that is  $Q = \Sigma_p V_A / 795$ , which is very similar to expression (7).

Observationally, saturation is seen in geomagnetic indices when they are plotted against solar wind driver functions. CPCP saturation formulas have a  $(1+Q)$  factor in the denominator that describes the reduction of the coupling. If one adds a factor of  $(1+Q)$  to the denominators of solar wind driver functions, much of the saturation behavior may be accounted for (or at least corrected for). This is shown in Figure 17, where we display the polar cap index (PCI) as functions of solar wind (a)  $vB_z$  and (b)  $vB_z/(1+Q)$ . The black points are individual hours of data and the red curves are 100-point running averages. Linear behavior is indicated by a dashed purple line placed such that the weakly driven data lie approximately on the line. Figure 17a shows a saturation of PCI at large values of  $vB_z$ , i.e., a strong deviation away from the dashed line, while Figure 17b shows less saturation with  $vB_z/(1+Q)$ . Although not shown, this behavior is even clearer for the auroral electrojet index AE. Much of the saturation behavior in the data can thus be accounted for (or removed) by the  $(1+Q)$  factor added to the denominator of the solar wind driver function.

It appears to the authors that (1) pressure balance considerations at the magnetopause, (2) the extent of the X-line, and (3) the properties of the magnetosheath flows are all important factors in determining the CPCP potential and its saturation level; all of these contribute to set the dayside reconnection rate and are strongly Mach number-dependent. The considerations of the Hill-Siscoe and Kivelson-Ridley models are somewhat different. Both involve the solar wind Alfvén speed (and thus Mach number) and its impact on magnetospheric current systems. The current physical interpretations of CPCP saturation have largely been based on results from global MHD simulations; although as noted above there may be numerical issues. Future work ought to try and discern between those interpretations on observational grounds.

### 3.8. Global sawtooth oscillations

Global sawtooth oscillations [e.g., *Huang, 2002; Henderson, 2004; Borovsky, 2004*] are periodic changes in the morphology of the storm-time magnetosphere wherein the magnetic field in the inner regions strongly stretches and then rapidly dipolarizes, together with energetic particle enhancements characteristic of magnetospheric substorms [*Sauvaud and Winckler, 1980*]. Whereas in the case of isolated substorms the stretching is confined to the nightside magnetosphere, during sawtooth oscillations the stretching extends through dawn and dusk to the dayside [*Cai et al., 2006; Clauer et al., 2006*].

*Borovsky and Denton [2006a]* found that global sawtooth oscillations tend to occur during higher-than-average solar wind Alfvén speeds. Performing a superposed epoch analysis of sawtooth oscillations, *Pulkkinen et al. [2007b]* found that these occur during somewhat lower-than-average Alfvén Mach number. Figure 1, introduced in section 3.1, shows this result in the fashion of an occurrence statistics distribution, using OMNI data during times of sawtooth oscillations, and in comparison with the distributions observed during other sorts of solar wind. This figure confirms that sawtooth oscillations tend to occur during low Mach number. This is compatible with sawtooth oscillations occurring primarily during CME-driven storms, by contrast to CIR-driven storms for which the Mach number is higher.

During global sawtooth oscillations the near-Earth magnetic field stretching that is typically observed during substorms (and storms) in the nightside magnetosphere occurs over a larger local time range. It extends Sunward of the terminator towards noon through the dawn and dusk sectors, although the stretching is typically smaller as one gets farther from midnight [c.f., *Borovsky, 2004; Cai et al., 2006*]. Figure 18 illustrates the connection between magnetic field stretching and Mach number from global MHD simulations. It shows 2D cuts of the plasma pressure with over-plotted sample magnetic field lines (red) in the dawn-dusk terminator plane (i.e., at  $X = 0 R_E$ ), for strong solar wind driving conditions with  $B_z = -15$  nT and  $|V| = 650$  km/s, but for (a) rather high ( $M_A = 6.88$ ) and (b) low ( $M_A = 1.99$ ) Mach numbers separately. These figures demonstrate that MHD simulations can qualitatively reproduce the stretching that spreads towards dusk and dawn during low Mach number, while the stretching is much smaller during high Mach number. The local time extension of the stretching towards the dayside is thus a low Mach number effect according to these MHD simulations.

While the present MHD simulations can reproduce such an extended stretching during low Mach number, which is characteristic of sawtooth oscillations, they are unable to reproduce the oscillations themselves, i.e., the loading and unloading cycle with a given periodicity. However, the very recent work by *Kuznetsova et al. [2007]*, using a global MHD simulation during low Mach number with non-gyrotropic corrections (implemented to the dissipation model in



the diffusion region) in the near-Earth tail region, was able to reproduce the periodic loading and unloading phases characteristic of sawtooth oscillations. The addition of this correction allowed for the periodic retreat and reformation of the near-Earth X-line in the code, thus leading to the periodic behavior of the stretching.

Stretching of the magnetic field on the nightside during typical substorms is associated with a squeezing of the plasma sheet by the lobe magnetic flux [*Birn and Schindler, 2002*]. The process by which stretching occurs towards dawn-dusk and the dayside, in the low Mach number regime during sawtooth oscillations, may be related to the presence of an enhanced polar cap oval (open field line area) together with enhanced lobe magnetic pressures. These may act to squeeze the dipole magnetosphere, and most substantially in the outer part of the magnetosphere in a way similar to that explained in the case of the midnight tail by *Birn and Schindler [2002]*, for instance. However, the exact processes that lead to wide (local time-wise) magnetic field stretching and to the periodic (loading-unloading) nature of sawtooth oscillations remain to be determined.

It must be mentioned that stretching in the inner magnetosphere in MHD simulations is possibly not realistic. This is because the stretching is related to the plasma pressure distribution in this region, which is controlled by magnetic drifts as well as electric drifts, but the former are not fully/explicitly described in the MHD framework (one should note the comment by *Vasyliunas [2004]* on this matter). It is therefore uncertain whether the stretching observed in MHD simulations is happening in a correct fashion.

Figure 1 shows that sawtooth oscillations tend to occur under low Mach number (observationally; see also *Borovsky and Denton [2006b]*) and the simulations of Figure 18 and of *Kuznetsova et al. [2007]* corroborate this relation. However, from observations it is difficult to determine whether sawtooth oscillations are due to the combination of a strong driving and a low Mach number, or are due to a strong driving only. This is due to the fact that strong driving often corresponds to low Mach number, as we will discuss in section 3.10. Sawtooth oscillations are much studied these days. Their relation to the solar wind Mach number, possibly through an altered interaction regime, ought to be further investigated.

### 3.9. Other expected effects

We primarily focused on some global alterations of solar wind – magnetosphere coupling during low Mach number. There likely are other alterations, both major and minor, that have not been presented here. In this section we describe a few other expected differences.

In the more extreme sub-Alfvénic regime ( $M_A < 1$ ) the solar wind – magnetosphere interaction changes even further. Large flows in the magnetosheath and asymmetric magnetopause shapes occur in a similar fashion. The polar cap tends

to saturate as well. A feature that further appears in the sub-Alfvénic regime is the Alfvén wing. Alfvén wings have been predicted, modeled and observed in the solar system [e.g., *Neubauer*, 1980; *Kivelson et al.*, 1997; *Linker et al.*, 1998; *Ridley*, 2007]. They are the result of Alfvén waves propagating away from the interaction region of a magnetized flow with a conducting obstacle, so as to form a cavity which geometry depends on the plasma flow speed compared to the Alfvén speed of the external wind (see *Neubauer* [1980] for details). Interestingly, *Ridley* [2007] recently showed from global MHD simulations that Alfvén wings at Earth do not suddenly appear when the Mach number just passes below  $M_A = 1$ , but rather that the magnetotail during super-Alfvénic solar wind consists of Alfvén wings that are essentially folded together. As the Mach number decreases the two Alfvén wings (from the northern and southern hemisphere) gradually separate from each other, and they eventually form totally separated and unconnected regions above and below the Earth for sub-Alfvénic flows. *Ridley* [2007] further suggests that the electric field in the Alfvén wings influences CPCP saturation, and may even be its origin in the framework of the generator-load model [*Kivelson and Ridley*, 2008]. We do not further discuss Alfvén wings and their impacts here. The reader is referred to *Ridley* [2007] where the details of related MHD simulation results may be found.

*Borovsky and Denton* [2006b] recently showed that during dayside plasmaspheric plume times the solar wind coupling with the magnetosphere is reduced (from the analysis of magnetospheric indices). They interpreted this to be the result of a reduction of magnetic reconnection owing to the high density of the plume plasma which decreases the local Alfvén speed at the dayside reconnection site. In the low Mach number regime, the dayside reconnection rate significantly decreases when the magnetospheric density increases, as observed in Eq. (3), as a result of  $\rho_m \gg \rho$  ( $\rho$  is the solar wind density and  $\rho_m$  the magnetospheric density). By contrast, in the high Mach number limit  $\rho$  may be comparable to  $\beta_s^{-1/2} \rho_m$  (Eq. (5); with  $\beta_s$  being the magnetosheath value), so that the relative effect of magnetospheric density should be reduced.

The occurrence and strength of the plasma depletion layer (PDL), which is known to form next to the dayside magnetopause in particular during northward IMF [e.g., *Zwan and Wolf*, 1976; *Phan et al.*, 1994], is expected to change as a function of Mach number. Although a detailed study is left aside here, this may easily be understood since the PDL formation process is a MHD effect. In the very high Mach number limit, the magnetic field is so insignificant that all flow properties become hydrodynamic-like [*Spreiter et al.*, 1966a; 1966b]. In this case the magnetic pile-up characteristic of the PDL may not exist.

The magnetospheric cusps are known to change position as a function of solar wind properties. Early statistics from the DMSP satellites have shown it moves equatorward (poleward) in response to solar wind pressure increase (decrease), as a result of its global expansion [*Newell and Meng*, 1994] (see also [*Yamauchi et al.*, 1996]). For

southward (northward) IMF orientation it moves equatorward (poleward) and for dawnward (duskward) IMF orientations it is displaced towards dawn (dusk) [Newell *et al.*, 1989]. As is further discussed in Borovsky *et al.* [2008b], we found that the Mach number also affects the cusp position in global MHD simulations. During times of CPCP saturation and low solar wind Mach number, the reduction in the dayside magnetic field strength leads the cusp to tilt sunward/equatorward.

Bow shock properties change during low Mach number solar wind. In addition to the decreased compression ratio, which affects the downstream magnetosheath densities and temperatures, the Mach number also changes the ion-to-electron temperature ratio [e.g., Thomsen *et al.*, 1985; Schwartz *et al.*, 1988]. The Earth's plasma sheet typically has a temperature ratio  $\sim 6-7$  [Baumjohann, 1993], which is also about that usually found in the magnetosheath [e.g., Paschmann *et al.*, 1993; Phan *et al.*, 1994]. It is thus often assumed that the temperature ratio in the plasma sheet is set by the ratio in the “source” magnetosheath and that the ratio is preserved as magnetosheath plasma is captured by the magnetosphere. This possibility may be tested as explained in section 4.

A low Mach number shock is also a weaker shock. It may lead to lower rates of particle reflection and weaker acceleration. This would affect the properties of the foreshock and any influence this region has on solar wind – magnetosphere coupling.

The level of turbulence and fluctuations is typically weaker in low  $\beta$  plasmas, owing to the stiffness of the magnetic field. Observationally, this is particularly true within magnetic clouds [e.g., Smith *et al.*, 2006]. This property is also likely to change the interaction of low Mach number CMEs with the magnetosphere [e.g., Borovsky and Funsten, 2003].

The asymmetries in magnetopause shape and the local time variations of magnetic stretching during storms and sawtooth oscillations will influence ring current and radiation belt particle drift properties and losses to the magnetopause. The ring current and radiation belt communities are indeed extensively working on realistic and self-consistent electromagnetic field models.

Finally, it is worth mentioning the article by Vasylunas [2004], which was dedicated to comparative magnetosphere studies and how these may give lessons for Earth. One of the points he raised is that the parameter  $Q$  may be used to discriminate between two regimes when “a magnetosphere” is solar wind-driven or ionosphere-driven (in a similar fashion to the distinctions originally made by Hill *et al.* [1976]). Some effects described in the present paper (such as CPCP saturation and possibly sawtooth oscillations) fall under such considerations, but a number of other effects (e.g., magnetosheath flows, magnetopause shape, etc.) primarily dependent on the solar wind Mach number.

### 3.10. Limitations from solar wind and ionospheric properties at Earth

For the Earth’s magnetosphere, one cannot easily use the existing solar wind and magnetospheric data to study coupling at low Mach number because the occurrence of low Mach number, CPCP saturation and strong driving are hard to decouple from each other. This is first illustrated in Figure 19a. Here the CPCP saturation parameter  $Q$  (expression (12)) is calculated for 93,070 hours of solar wind measurements from the OMNI dataset using available  $F_{10.7}$  values. This hourly  $Q$  value is plotted (black points) as a function of solar wind Mach number. A 100-point running average is plotted in red. When the Mach number is low (say,  $M_A < 2.5$ ), the CPCP tends to be saturated (say,  $Q > 2$ ). As explained previously in section 3.7, this is simply because low Mach number and high  $Q$  values both tend to occur when the Alfvén speed of the solar wind is high, while the effect of conductivity is more limited at Earth. A major limitation in studying strong driving periods is that during strong driving the Mach number tends to be low and CPCP tends to saturate. This is shown in Figure 19b where the parameter  $Q$  is plotted (black points) as a function of solar wind electric field ( $vB_z$ ) “driving”, and again a 100-point running average is plotted in red. As can be seen, at the strongest levels of driving the polar cap tends saturate; not because of strong driving, but because low Mach number tends to occur when the solar wind magnetic field is large, which is when strong driving occurs. One thus cannot either study solar wind – magnetosphere coupling at low Mach number without considering strong driving, as is illustrated in the same fashion in Figure 19c. If there were instances of superfast solar wind with modest magnetic field strengths, or if there were a larger range of ionospheric conductivity at Earth, then one could study times of low Mach number, strong driving and CPCP saturation separately. Unfortunately, the three panels of Figure 19 demonstrate that at Earth, low Mach number, CPCP saturation, and strong driving all tend to occur during the same periods, i.e., during CME-driven storms.

## 4. Summary and future work

### 4.1 Summary

We illustrated some fundamental alterations of the solar wind – magnetosphere interaction that occur during low Mach number solar wind. We showed that low Mach number conditions primarily occur during coronal mass ejections (CMEs) and the subset of Magnetic clouds in particular. The ensemble of these phenomena is likely very important for solar wind – magnetosphere interaction during CME driven storms, in addition to the phenomena that occur in the well-studied magnetotail and inner magnetosphere. The occurrence of these effects is mediated by the magnetosheath, which properties in terms of thermal  $\beta$  value (lower) and flow pattern are significantly altered during low Mach number. In summary the primary effects that influence magnetospheric dynamics are as follows.

- Asymmetric magnetosheath flows with substantial enhancements on the flanks for IMF orientations predominantly northward or southward. The location of the flows follows the IMF orientation so that for horizontal IMF the enhanced flows are displaced towards the poles. The magnitude of the enhanced flows increases as the Mach number decreases. It can reach values significantly larger than the speed of the solar wind itself, and although the magnetosheath is thicker under such conditions.
- Asymmetric magnetopause and magnetotail shapes with a larger radius in the north-south direction as compared to the dawn-dusk direction when the IMF is directed northward or southward. This asymmetry is stronger during southward IMF, and it follows the IMF orientation so that for horizontal IMF the dawn-dusk radius should be larger.
- Changes in the development of the Kelvin-Helmholtz instability (e.g., faster wave growth) may be expected during low Mach number solar wind owing to the increased velocities in the magnetosheath just adjacent to the magnetopause. As suggested by *Rosenqvist et al.* [2007], these may in turn lead to giant spiral auroral features.
- The factors controlling dayside magnetic reconnection vary with solar wind Mach number. By use of the dayside reconnection rate function constructed by *Borovsky* [2008], we could show the occurrence of a “density” effect which results from a strong “positive” dependence of the reconnection rate on solar wind density, but in the low Mach number regime only.
- Both cross polar cap potential (CPCP) saturation and Alfvén wings are expected to occur during low Mach number solar wind. This topic is currently a widely studied one. There is a consensus on the fact that CPCP occurs, but not on its physical interpretation. Processes involving the limited conductance of the solar wind generator, which is dependent upon the Alfvén Mach number, may be a fundamental aspect of CPCP saturation.
- Global sawtooth oscillations statistically tend to occur more often during low Mach number solar wind. Global MHD simulations show that the magnetospheric field stretching observed at the terminator is stronger during low Mach number for a similar value of the “driving” electric field. The physical reasons for this increased stretching are at present not well understood.

#### 4.2 Future work

Numerous investigations should be done to complete the present study and confirm the effects described. Below we list a few topics that ought to be addressed in the future.

- Confirmation of magnetosheath flow and magnetopause asymmetries should be performed in a statistical fashion, for instance by using data from the Cluster spacecraft fleet which has a polar orbit and samples this region during significant parts of its orbit.

- Future studies ought to focus on quantifying a possible increase in growth rate of the Kelvin-Helmholtz instability at the magnetopause during low Mach number conditions. This might be done using data from global MHD simulations when these have high-enough resolution (see section 3.5 for details). This may otherwise be done by a combined use of global simulations (giving the large-scale structure of the flows) and local simulations (allowing for detailed investigation of the growth and other properties such as plasma transport, and preferably in three dimensions to account for the effect of magnetic tension forces).
- The “density” effect on the dayside reconnection rate described in this paper for low Mach number has been suggested from simulations. It requires, as well as the general trends observed in the coupling function of *Borovsky* [2008], to be confirmed by observations. It is known, however, that determination of the reconnection rate from in situ spacecraft measurements is not easy.
- Because CPCP saturation is a global, large-scale process, global MHD simulations have been extensively used to investigate its origin. However, it is unsure whether the saturation observed in global MHD simulations necessarily reflects reality. Appropriate observational studies are needed to further our understanding on this topic. Due to the limitations of solar wind and ionospheric properties at Earth, the study of other systems may be a key (cf. below).
- *Kuznetsova et al.* [2007], using a non-gyrotropic correction (implemented to their dissipation model in the diffusion region) in the near-Earth tail region, were able to reproduce the periodicity associated with sawtooth oscillations in a global MHD simulation for the first time. They worked in a low Mach number solar wind regime, which they assumed are the conditions prevailing during sawtooth oscillations. It would be of interest in the future to use the same model and check whether the periodic behavior they observed may appear during high Mach number conditions as well.
- The ion-to-electron temperature ratio in the magnetosheath is predicted to be lower than 6-7 for low Mach number solar wind. An interesting test of the solar wind/magnetosheath origin of the plasma sheet is to examine the temperature ratio in the plasma sheet during such conditions as well. If the plasma sheet temperature ratio is lower, then evidence supporting plasma entry mechanisms that preserve the ratio are supported. If the plasma sheet temperature ratio remains high, then evidence supporting the notion that the plasma entry mechanism forces the ratio is obtained.

Finally, spacecraft observations have shown that closer to the Sun the solar wind may typically have a lower Mach number than at Earth. Most of the effects described here are thus expected to occur more commonly in the interaction between the solar wind and Mercury’s magnetosphere. In addition, Mercury does not have an ionosphere. This suggests that the behavior of magnetospheric convection will largely differ (e.g., *Vasyliunas* [2004], see also *Fujimoto et al.* [2007] for a review on Mercury’s magnetosphere). Mercury constitutes a different regime from which to learn, since both solar wind and ionospheric properties differ from those at Earth. Analysis of data from Messenger and Bepi-

Colombo should allow us to test our understanding of all these low Mach number effects. These effects are to be expected at other astronomical bodies where an external low Mach number flow prevails.

**Acknowledgments.** The authors thank J. Birn, M. Denton, T. Phan, J. Drake, M. Thomsen, A. Ridley, J. Raeder, T. Pulkkinen, R. Skoug, and R. Lopez for fruitful discussions. We also especially thank J. Kozyra for the use of the list of spiral auroral features during intense storms. We are most grateful to the Community Coordinated Modeling Center at NASA Goddard Space Flight Center (<http://ccmc.gsfc.nasa.gov>) and especially to M. Kuznetsova, A. Chulaki, L. Rastaetter, and M. Hesse for their help with some special runs used in this study. We also thank OMNIWeb for the use of OMNI solar wind data and the National Geophysical Data Center for the use of  $F_{10.7}$  data. Work at Los Alamos was performed under the auspices of the US Department of Energy, with support from NSF (Geospace Environment Modeling and National Space Weather Program) and NASA programs (Guest Investigator and Living With a Star TR&T). We also thank the reviewers for their constructive comments.

## References

- Avanov, L. A., V. N. Smirnov, J. H. Waite Jr., S. A. Fuselier, and O. L. Vaisberg (2001), High-latitude magnetic reconnection in sub-Alfvénic flow: Interball Tail observations on May 29, 1996, *J. Geophys. Res.*, 106(A12), 29,491–29,502.
- Baumjohann, W. (1993), The near-Earth plasma sheet: An AMPTE/IRM perspective, *Space Sci. Rev.*, 64, 141.
- Biernat H. K., N. V. Erkaev, C. J. Farrugia, D. F. Vogl, and W. Schaffnerberger (2000), MHD effects of the solar wind flow around planets, *Nonlin. Proc. Geophys.*, 7(3-4), 201-209.
- Birn, J., et al. (2001), Geospace Environmental Modeling (GEM) Magnetic Reconnection Challenge, *J. Geophys. Res.*, 106(A3), 3715–3719.
- Birn, J., and K. Schindler (2002), Thin current sheets in the magnetotail and the loss of equilibrium, *J. Geophys. Res.*, 107(A7), 1117, doi:10.1029/2001JA000291.
- Boardsen, S. A., T. E. Eastman, T. Sotirelis, and J. L. Green (2000), An empirical model of the high-latitude magnetopause, *J. Geophys. Res.*, 105, 23193.
- Borovsky, J. E., and H. O. Funsten (2003), Role of solar wind turbulence in the coupling of the solar wind to the Earth's magnetosphere, *J. Geophys. Res.*, 108(A6), 1246, doi:10.1029/2002JA009601.
- Borovsky, J. (2004), Global Sawtooth Oscillations of the Magnetosphere, *Eos Trans. AGU*, 85(49), 525.
- Borovsky, J. E., and M. H. Denton (2006a), Differences between CME-driven storms and CIR-driven storms, *J. Geophys. Res.*, 111, A07S08, doi:10.1029/2005JA011447.
- Borovsky, J. E., and M. H. Denton (2006b), Effect of plasmaspheric drainage plumes on solar-wind/magnetosphere coupling, *Geophys. Res. Lett.*, 33, L20101, doi:10.1029/2006GL026519.
- Borovsky, J. E., and J. T. Steinberg (2006), The “calm before the storm” in CIR/magnetosphere interactions: Occurrence statistics, solar wind statistics, and magnetospheric preconditioning, *J. Geophys. Res.*, 111, A07S10, doi:10.1029/2005JA011397.
- Borovsky, J. E., and M. Hesse (2007), The reconnection of magnetic fields between plasmas with different densities: Scaling relations, *Phys. Plasmas*, 14, 102309.
- Borovsky, J. E. (2008), The rudiments of a theory of solar-wind/magnetosphere coupling derived from first principles, *J. Geophys. Res.*, in press.
- Borovsky, J. E., M. Hesse, J. Birn, and M. M. Kuznetsova (2008a), What determines the reconnection rate at the dayside magnetosphere?, *J. Geophys. Res.*, 113, A07210, doi:10.1029/2007JA012645.
- Borovsky, J. E., B. Lavraud, and M. M. Kuznetsova (2008b), Polar-cap saturation, dayside reconnection and changes to the magnetosphere, *J. Geophys. Res.*, in press.
- Burton, R. K., R. L. McPherron, and C. T. Russell (1975), An Empirical Relationship Between Interplanetary Conditions and *Dst*, *J. Geophys. Res.*, 80(31), 4204–4214.
- Cai, X., M. G. Henderson, and C. R. Clauer (2006), A statistical study of magnetic dipolarization for sawtooth events and isolated substorms at geosynchronous orbit with GOES data, *Ann. Geophys.*, 24(12), 3481-3490.
- Cane, H. V., and I. G. Richardson, Interplanetary coronal mass ejections in the near-Earth solar wind during 1996-2002 (2003), *J. Geophys. Res.*, 108, 1156, No. A4, doi:10.1029/2002JA009817.
- Cassak, P. A., and M. A. Shay (2007), Scaling of asymmetric magnetic reconnection in collisional plasmas, *Phys. Plasmas*, submitted.
- Chandrasekhar, S. (1961), Hydrodynamic and hydromagnetic Stability, *Oxford University Press*, New York.
- Chen, S.-H., M. G. Kivelson, J. T. Gosling, R. J. Walker, and A. J. Lazarus (1993), Anomalous Aspects of Magnetosheath Flow and of the Shape and Oscillations of the Magnetopause During an Interval of Strongly Northward Interplanetary Magnetic Field, *J. Geophys. Res.*, 98(A4), 5727–5742.
- Clauer, C. R., X. Cai, D. Welling, A. DeJong, and M. G. Henderson (2006), Characterizing the 18 April 2002 storm-time sawtooth events using ground magnetic data, *J. Geophys. Res.*, 111, A04S90, doi:10.1029/2005JA011099.
- Dmitriev, A. V., and A. V. Suvorova (2000), Three-dimensional artificial neural network model of the dayside magnetopause, *J. Geophys. Res.*, 105, 18909.
- Dmitriev, A. V., A. V. Suvorova, J. K. Chao, and Y.-H. Yang (2004), Dawn-dusk asymmetry of geosynchronous magnetopause crossings, *J. Geophys. Res.*, 109, A05203, doi:10.1029/2003JA010171.
- Drell, S. D., H. M. Foley, and M. A. Ruderman (1965), Drag and Propulsion of Large Satellites in the Ionosphere: An Alfvén Propulsion Engine in Space, *J. Geophys. Res.*, 70(13), 3131–3145.
- Farrugia, C. J., N. V. Erkaev, H. K. Biernat, and L. F. Burlaga (1995), Anomalous Magnetosheath Properties During Earth Passage of an Interplanetary Magnetic Cloud, *J. Geophys. Res.*, 100(A10), 19,245–19,257.

- Farrugia, C. J., H. J. Singer, D. Evans, D. Berdichevsky, J. D. Scudder, K. W. Ogilvie, R. J. Fitzenreiter, and C. T. Russell (2000), Response of the Equatorial and Polar Magnetosphere to the Very Tenuous Solar Wind on May 11, 1999, *Geophys. Res. Lett.*, 27(23), 3773–3776.
- Farrugia, C. J., F. T. Gratton, V. K. Jordanova, H. Matsui, S. Mühlbachler, R. B. Torbert, K. W. Ogilvie and H. J. Singer (2008), Tenuous solar winds: Insights on solar wind–magnetosphere interactions, *J. Atmos. Solar Terr. Phys.*, 70(2–4), 371–376.
- Fairfield, D. H., A. Otto, T. Mukai, S. Kokubun, R. P. Lepping, J. T. Steinberg, A. J. Lazarus, and T. Yamamoto (2000), Geotail observations of the Kelvin-Helmholtz instability at the equatorial magnetotail boundary for parallel northward fields, *J. Geophys. Res.*, 105(A9), 21,159–21,174.
- Fairfield, D. H., H. C. Iver, M. D. Desch, A. Szabo, A. J. Lazarus, and M. R. Aellig (2001), The location of low Mach number bow shocks at Earth, *J. Geophys. Res.*, 106(A11), 25,361–25,376.
- Fairfield, D. H., M. M. Kuznetsova, T. Mukai, T. Nagai, T. I. Gombosi, and A. J. Ridley (2007), Waves on the dusk flank boundary layer during very northward interplanetary magnetic field conditions: Observations and simulation, *J. Geophys. Res.*, 112, A08206, doi:10.1029/2006JA012052.
- Fedder, J. A., and J. G. Lyon (1995), The Earth's Magnetosphere is 165  $R_E$  Long: Self-Consistent Currents, Convection, Magnetospheric Structure, and Processes for Northward Interplanetary Magnetic Field, *J. Geophys. Res.*, 100(A3), 3623–3635.
- Formisano, V., V. Domingo, and K. P. Wenzel (1979), The three-dimensional shape of the magnetopause, *Planet. Space Sci.*, 27, 1137.
- Freeman, M. P., and C. J. Farrugia (1999), Solar wind input between substorm onsets during and after the October 18–20, 1995, magnetic cloud, *J. Geophys. Res.*, 104(A10), 22,729–22,744.
- Fujimoto, M., and T. Terasawa (1994), Anomalous Ion Mixing within an MHD Scale Kelvin-Helmholtz Vortex, *J. Geophys. Res.*, 99(A5), 8601–8613.
- Fujimoto, M., W., Baumjohann, K. Kabin, R. Nakamura, J. A. Slavin, N. Terada, and L. Zelenyi (2007), Hermean magnetosphere-solar wind interaction, *Space Sci. Rev.*, 132(2–4), 529–550.
- Fuselier, S. A., S. M. Petriner, and K. J. Trattner (2000), Stability of the High-Latitude Reconnection Site for Steady Northward IMF, *Geophys. Res. Lett.*, 27(4), 473–476.
- Fuselier, S. A., K. J. Trattner, S. M. Petriner, C. J. Owen, and H. Rème (2005), Computing the reconnection rate at the Earth's magnetopause using two spacecraft observations, *J. Geophys. Res.*, 110, A06212, doi:10.1029/2004JA010805.
- Goertz, C. K., and R. W. Boswell (1979), Magnetosphere-ionosphere coupling, *J. Geophys. Res.*, 84, 7239.
- Goertz, C. K., L.-H. Shan, and R. A. Smith (1993), Prediction of Geomagnetic Activity, *J. Geophys. Res.*, 98(A5), 7673–7684.
- Gombosi, T. I., et al. (2000), Multiscale MHD simulation of a coronal mass ejection and its interaction with the magnetosphere-ionosphere system, *J. Atmos. Solar-Terr. Phys.*, 62, No.16, 1515–1525.
- Gonzalez, W. D., and A. L. C. Gonzalez (1984), Energy transfer by magnetopause reconnection and the substorm parameter  $\epsilon$ , *Planet. Space Sci.*, 32, 1007.
- Gonzalez, W. D., and F. S. Mozer (1974), A Quantitative Model for the Potential Resulting from Reconnection with an Arbitrary Interplanetary Magnetic Field, *J. Geophys. Res.*, 79(28), 4186–4194.
- Gosling, J. T., D. N. Baker, S. J. Bame, W. C. Feldman, R. D. Zwickl, and E. J. Smith (1987), Bidirectional solar wind electron heat flux events, *J. Geophys. Res.*, 92, 8519–8535.
- Gosling, J. T. (1990), Coronal mass ejections and magnetic flux ropes in interplanetary space, in *Physics of Magnetic Flux Ropes*, *Geophys. Monogr. Ser.*, vol. 58, edited by C. T. Russell, E. R. Priest, and L. C. Lee, 343–364, AGU, Washington, D.C..
- Hairston, M. R., K. A. Drake, and R. Skoug (2005), Saturation of the ionospheric polar cap potential during the October–November 2003 superstorms, *J. Geophys. Res.*, 110, A09S26, doi:10.1029/2004JA010864.
- Hasegawa, H., M. Fujimoto, T. D. Phan, H. Rème, A. Balogh, M. W. Dunlop, C. Hashimoto, and R. TanDokoro (2004), Transport of solar wind into Earth's magnetosphere through rolled-up Kelvin-Helmholtz vortices, *Nature*, 430, 755–758.
- Hasegawa, H., M. Fujimoto, K. Takagi, Y. Saito, T. Mukai, and H. Rème (2006), Single-spacecraft detection of rolled-up Kelvin-Helmholtz vortices at the flank magnetopause, *J. Geophys. Res.*, 111, A09203, doi:10.1029/2006JA011728.
- Henderson, M. G. (2004), The May 2–3, 1986 CDAW-9C interval: A sawtooth event, *Geophys. Res. Lett.*, 31, L11804, doi:10.1029/2004GL019941.
- Hill, T. W., A. J. Dessler, and R. A. Wolf (1976), Mercury and Mars: The role of ionospheric conductivity in the acceleration of magnetospheric particles, *Geophys. Res. Lett.*, 3, 429–432.
- Howe, H. C., and J. H. Binsack (1972), Explorer 33 and 35 plasma observations of magnetosheath flow, *J. Geophys. Res.*, 77, No.19, 3334–3344.
- Huang, C. (2002), Evidence of periodic (2–3 hour) near-tail magnetic reconnection and plasmoid formation: Geotail observations, *Geophys. Res. Lett.*, 29(24), 2189, doi:10.1029/2002GL016162.
- Hughes, W. F., and F. J. Young (1966), *The Electrodynamics of Fluids*, Ch. 12, Wiley, New York.
- Jian, L., C. T. Russell, J. G. Luhmann, and R. M. Skoug (2006), Properties of interplanetary Coronal Mass Ejections at one AU during 1995–2004, *Solar Phys.*, 239(1–2), 393–436.
- Kan, J. R., and L. C. Lee (1979), Energy Coupling Function and Solar Wind-Magnetosphere Dynamo, *Geophys. Res. Lett.*, 6(7), 577–580.
- Kataoka, R., D. H. Fairfield, D. G. Sibeck, L. Rastätter, M.-C. Fok, T. Nagatsuma, and Y. Ebihara (2005), Magnetosheath variations during the storm main phase on 20 November 2003: Evidence for solar wind density control of energy transfer to the magnetosphere, *Geophys. Res. Lett.*, 32, L21108, doi:10.1029/2005GL024495.
- Kawano, H., S. M. Petriner, C. T. Russell, and T. Higuchi (1999), Magnetopause shape determinations from measured position and estimated flaring angle, *J. Geophys. Res.*, 104(A1), 247–261.
- King, J. H., and N. E. Papitashvili (2005), Solar wind spatial scales in and comparisons of hourly Wind and ACE plasma and magnetic field data, *J. Geophys. Res.*, 110(A2), A02209, doi:10.1029/2004JA010804.
- Kivelson, M. G., K. K. Khurana, F. V. Coroniti, S. Joy, C. T. Russell, R. J. Walker, J. Warnecke, L. Bennett, and C. Polanskey (1997), The Magnetic Field and Magnetosphere of Ganymede, *Geophys. Res. Lett.*, 24(17), 2155–2158.
- Kivelson, M. G., and A. J. Ridley (2008), Saturation of the polar cap potential: Inference from Alfvén wing arguments, *J. Geophys. Res.*, doi:10.1029/2007JA012302, in press.
- Kuznetsova, M. M., M. Hesse, L. Rastätter, A. Taktakishvili, G. Toth, D. L. De Zeeuw, A. Ridley, and T. I. Gombosi (2007), Multiscale modeling of magnetospheric reconnection, *J. Geophys. Res.*, 112, A10210, doi:10.1029/2007JA012316.



- Lai, S. H., and L. H. Lyu (2006), Nonlinear evolution of the MHD Kelvin-Helmholtz instability in a compressible plasma, *J. Geophys. Res.*, 111, A01202, doi:10.1029/2004JA010724.
- Lavraud, B., et al. (2004), The exterior cusp and its boundary with the magnetosheath: Cluster multi-event analysis, *Ann. Geophys.*, 22, No. 8, 3039-3054.
- Lavraud, B., M. F. Thomsen, M. G. G. T. Taylor, Y. L. Wang, T. D. Phan, S. J. Schwartz, R. C. Elphic, A. Fazakerley, H. Rème, and A. Balogh (2005), Characteristics of the magnetosheath electron boundary layer under northward interplanetary magnetic field: Implications for high-latitude reconnection, *J. Geophys. Res.*, 110, A06209, doi:10.1029/2004JA010808.
- Lavraud, B., M. F. Thomsen, B. Lefebvre, S. J. Schwartz, K. Seki, T. D. Phan, Y. L. Wang, A. Fazakerley, H. Rème, and A. Balogh (2006), Evidence for newly closed magnetosheath field lines at the dayside magnetopause under northward IMF, *J. Geophys. Res.*, 111, A05211, doi:10.1029/2005JA011266.
- Lavraud, B., J. E. Borovsky, A. J. Ridley, E. W. Pogue, M. F. Thomsen, H. Rème, A. N. Fazakerley, and E. A. Lucek (2007), Strong bulk plasma acceleration in Earth's magnetosheath: A magnetic slingshot effect?, *Geophys. Res. Lett.*, 34, L14102, doi:10.1029/2007GL030024.
- Le, G., C. T. Russell, and S. M. Petrinec (2000), The magnetosphere on May 11, 1999, the day the solar wind almost disappeared: I. Current systems, *Geophys. Res. Lett.*, 27(13), 1827-1830.
- Lei, W., R. Gendrin, B. Higel, and J. Berchem (1981), Relationships between the Solar Wind Electric Field and the Magnetospheric Convection Electric Field, *Geophys. Res. Lett.*, 8(10), 1099-1102.
- Lepping, R. P., D. B. Berdichevsky, C.-C. Wu, A. Szabo, T. Narock, F. Mariani, A. J. Lazarus, and A. J. Quivers (2006), A Summary of WIND Magnetic Clouds for the Years 1995 - 2003: Model-Fitted Parameters, Associated Errors, and classifications, *Ann. Geophys.*, 24(1), 215-245.
- Li, W., J. Raeder, J. Dorelli, M. Øieroset, and T. D. Phan (2005), Plasma sheet formation during long period of northward IMF, *Geophys. Res. Lett.*, 32, L12S08, doi:10.1029/2004GL021524.
- Li, W., J. Raeder, M. F. Thomsen, and B. Lavraud (2008), Solar wind plasma entry into the magnetosphere under northward IMF conditions, *J. Geophys. Res.*, doi:10.1029/2007JA012604, in press.
- Liemohn, M. W., and A. J. Ridley (2002), Comment on "Nonlinear response of the polar ionosphere to large values of the interplanetary electric field" by C. T. Russell et al., *J. Geophys. Res.*, 107(A12), 1460, doi:10.1029/2002JA009440.
- Linker, J. A., K. K. Khurana, M. G. Kivelson, and R. J. Walker (1998), MHD simulations of Io's interaction with the plasma torus, *J. Geophys. Res.*, 103(E9), 19,867-19,877.
- Lopez, R. E., M. Wiltberger, S. Hernandez, and J. G. Lyon (2004), Solar wind density control of energy transfer to the magnetosphere, *Geophys. Res. Lett.*, 31, L08804, doi:10.1029/2003GL018780.
- Maltsev, Y. P., W. B. Lyatsky, and A. M. Lyatskaya (1977), Currents over the auroral arc, *Planet. Space Sci.*, 25, 53.
- Matsumoto, Y., and M. Hoshino (2006), Turbulent mixing and transport of collisionless plasmas across a stratified velocity shear layer, *J. Geophys. Res.*, 111, A05213, doi:10.1029/2004JA010988.
- Matsumoto, Y., and K. Seki (2007), The secondary instability initiated by the three-dimensional nonlinear evolution of the Kelvin-Helmholtz instability, *J. Geophys. Res.*, 112, A06223, doi:10.1029/2006JA012114.
- Merkine, V. G., K. Papadopoulos, G. Milikh, A. S. Sharma, X. Shao, J. Lyon, and C. Goodrich (2003), Effects of the solar wind electric field and ionospheric conductance on the cross polar cap potential: Results of global MHD modeling, *Geophys. Res. Lett.*, 30(23), 2180, doi:10.1029/2003GL017903.
- Merkin, V. G., A. S. Sharma, K. Papadopoulos, G. Milikh, J. Lyon, and C. Goodrich (2005), Global MHD simulations of the strongly driven magnetosphere: Modeling of the transpolar potential saturation, *J. Geophys. Res.*, 110, A09203, doi:10.1029/2004JA010993.
- Michel, F. C., and A. J. Dessler (1970), Diffusive Entry of Solar-Flare Particles into Geomagnetic Tail, *J. Geophys. Res.*, 75(31), 6061-6072.
- Nagatsuma, T. (2004), Conductivity dependence of cross-polar potential saturation, *J. Geophys. Res.*, 109, A04210, doi:10.1029/2003JA010286.
- Neubauer, F. M. (1980), Nonlinear standing Alfvén wave current system at Io: Theory, *J. Geophys. Res.*, 85(A3), 1171-1178.
- Newell, P. T., C. I. Meng, D. G. Sibeck, and P. Lepping (1989), Some low-altitude cusp dependencies on the interplanetary magnetic field, *J. Geophys. Res.*, 94, 8921.
- Newell, P. T., and C. I. Meng (1994), Ionospheric projections of magnetospheric regions under low and high solar wind pressure conditions, *J. Geophys. Res.*, 99, 273.
- Newell, P. T., T. Sotirelis, K. Liou, C.-I. Meng, and F. J. Rich (2007), A nearly universal solar wind-magnetosphere coupling function inferred from 10 magnetospheric state variables, *J. Geophys. Res.*, 112, A01206, doi:10.1029/2006JA012015.
- Nykyri, K., and A. Otto (2001), Plasma Transport at the Magnetospheric Boundary due to Reconnection in Kelvin-Helmholtz Vortices, *Geophys. Res. Lett.*, 28(18), 3565-3568.
- Ober, D. M., N. C. Maynard, and W. J. Burke (2003), Testing the Hill model of transpolar potential saturation, *J. Geophys. Res.*, 108(A12), 1467, doi:10.1029/2003JA010154.
- Ogino, T., R. J. Walker, and M. Ashour-Abdalla (1994), A Global Magnetohydrodynamic Simulation of the Response of the Magnetosphere to a Northward Turning of the Interplanetary Magnetic Field, *J. Geophys. Res.*, 99(A6), 11,027-11,042.
- Øieroset, M., J. Raeder, T. D. Phan, S. Wing, J. P. McFadden, W. Li, M. Fujimoto, H. Rème, and A. Balogh (2005), Global cooling and densification of the plasma sheet during an extended period of purely northward IMF on October 22-24, 2003, *Geophys. Res. Lett.*, 32, L12S07, doi:10.1029/2004GL021523.
- Onsager, T. G., J. D. Scudder, M. Lockwood, and C. T. Russell (2001), Reconnection at the high-latitude magnetopause during northward interplanetary magnetic field conditions, *J. Geophys. Res.*, 106(A11), 25,467-25,488.
- Otto, A., and D. H. Fairfield (2000), Kelvin-Helmholtz instability at the magnetotail boundary: MHD simulation and comparison with Geotail observations, *J. Geophys. Res.*, 105(A9), 21,175-21,190.
- Parker, E. N. (1973), The reconnection rate of magnetic fields, *Astrophys. J.*, 180, 247.
- Paschmann, G., W. Baumjohann, N. Scopke, T. -D. Phan, and H. Lühr (1993), Structure of the Dayside Magnetopause for Low Magnetic Shear, *J. Geophys. Res.*, 98(A8), 13,409-13,422.
- Perreault, P., and S.-I. Akasofu (1978), A study of geomagnetic storms, *Geophys. J. R. Astron. Soc.*, 54, 547-573.
- Petrinec, S. M., and C. T. Russell (1996), Near-Earth magnetotail shape and size as determined from the magnetopause flaring angle, *J. Geophys. Res.*, 101(A1), 137-152.

- Petrinec, S. M., T. Mukai, A. Nishida, T. Yamamoto, T. K. Nakamura, and S. Kokubun (1997), Geotail observations of magnetosheath flow near the magnetopause, using Wind as a solar wind monitor, *J. Geophys. Res.*, 102(A12), 26,943–26,959.
- Phan, T.-D., G. Paschmann, W. Baumjohann, N. Sckopke, and H. Lühr (1994), The Magnetosheath Region Adjacent to the Dayside Magnetopause: AMPTE/IRM Observations, *J. Geophys. Res.*, 99(A1), 121–141.
- Pudovkin, M.I., S. A. Zaitseva, T. A. Bazhenova, and V. G. Andrezen (1985), Electric fields and currents in the Earth's polar caps, *Planet. Space Sci.*, 33, 407.
- Pulkkinen, T. I., C. C. Goodrich, and J. G. Lyon (2007a), Solar wind electric field driving of magnetospheric activity: Is it velocity or magnetic field?, *Geophys. Res. Lett.*, 34, L21101, doi:10.1029/2007GL031011.
- Pulkkinen, T. I., N. Partamies, R. L. McPherron, M. Henderson, G. D. Reeves, M. F. Thomsen, and H. J. Singer (2007b), Comparative statistical analysis of storm time activations and sawtooth events, *J. Geophys. Res.*, 112, A01205, doi:10.1029/2006JA012024.
- Raeder, J., J. Berchem, M. Ashour-Abdalla, L. A. Frank, W. R. Paterson, K. L. Ackerson, S. Kokubun, T. Yamamoto, and J. A. Slavin (1997), Boundary Layer Formation in the Magnetotail: Geotail Observations and Comparisons with a Global MHD Simulation, *Geophys. Res. Lett.*, 24(8), 951–954.
- Raeder, J., and G. Lu (2005), Polar cap potential saturation during large geomagnetic storms, *Adv. Space Res.*, 36(10), 1804–1808.
- Ramo, S., J. R. Whinnery, and T. van Duzer (1984), *Fields and Waves in Communication Electronics*, Sect. 5.2, Wiley, New York.
- Reiff, P. H., R. W. Spiro, and T. W. Hill (1981), Dependence of Polar Cap Potential Drop on Interplanetary Parameters, *J. Geophys. Res.*, 86(A9), 7639–7648.
- Reiff, P. H., and J. G. Luhmann (1986), Solar wind control of the polar-cap voltage, in *Solar Wind-Magnetosphere Coupling*, Y. Kamide and J. A. Slavin (eds.), pg. 453, Terra Scientific, Tokyo.
- Ridley, A. J., T. I. Gombosi, and D. L. DeZeeuw (2004), Ionospheric control of the magnetosphere: conductance, *Ann. Geophys.*, 22, No.2, 567–584.
- Ridley, A. J. (2005), A new formulation for the ionospheric cross polar cap potential including saturation effects, *Ann. Geophys.*, 23(11), 3533–3547.
- Ridley, A. J. (2007), Alfvén wings at Earth's magnetosphere under strong interplanetary magnetic fields, *Ann. Geophys.*, 25(2), 533–542.
- Rosenqvist, L., A. Kullen, and S. Buchert (2007), An unusual giant spiral arc in the polar cap region during the northward phase of a Coronal Mass Ejection, *Ann. Geophys.*, 25, 507–517.
- Rosenqvist, L., A. Vaivads, A. Retinò, T. Phan, H. J. Opgenoorth, I. Dandouras, and S. Buchert (2008), Modulated reconnection rate and energy conversion at the magnetopause under steady IMF conditions, *Geophys. Res. Lett.*, 35, L08104, doi:10.1029/2007GL032868.
- Russell, C. T., and S. M. Petrinec (1996), Comments on "Towards an MHD Theory for the Standoff Distance of Earth's Bow shock" by I.H. Cairns and C.L. Grabbe, *Geophys. Res. Lett.*, 23(3), 309–310.
- Russell, C. T. (2000), The solar wind interaction with the Earth's magnetosphere: A tutorial, *IEEE Trans. Plasma Sci.*, 28, 1818.
- Russell, C. T., J. G. Luhmann, and G. Lu (2001), Nonlinear response of the polar ionosphere to large values of the interplanetary electric field, *J. Geophys. Res.*, 106, 18,496–18,504.
- Sauvaud, J.-A., and J. R. Winckler (1980), Dynamics of Plasma, Energetic Particles, and Fields Near Synchronous Orbit in the Nighttime Sector During Magnetospheric Substorms, *J. Geophys. Res.*, 85(A5), 2043–2056.
- Schindler, K., M. Hesse, and J. Birn (1988), General Magnetic Reconnection, Parallel Electric Fields, and Helicity, *J. Geophys. Res.*, 93(A6), 5547–5557.
- Scholer, M. (1970), On the motion of artificial ion clouds in the magnetosphere, *Planet. Space Sci.*, 18, 977.
- Schwartz, S. J., M. F. Thomsen, S. J. Bame, and J. Stansberry (1988), Electron Heating and the Potential Jump Across Fast Mode Shocks, *J. Geophys. Res.*, 93(A11), 12,923–12,931.
- Scurry, L., and C. T. Russell (1991), Proxy Studies of Energy Transfer to the Magnetosphere, *J. Geophys. Res.*, 96(A6), 9541–9548.
- Shepherd, S. G. (2007), Polar cap potential saturation: Observations, theory, and modeling, *J. Atmos. Solar-Terr. Phys.*, 69(3), 234–248.
- Shue, J.-H., J. K. Chao, H. C. Fu, C. T. Russell, P. Song, K. K. Khurana, and H. J. Singer (1997), A new functional form to study the solar wind control of the magnetopause size and shape, *J. Geophys. Res.*, 102(A5), 9497–9511.
- Shue, J.-H., and P. Song (2002), The location and shape of the magnetopause, *Planet. Space Sci.*, 50(5–6), 549–558.
- Sibeck, D. G., G. L. Siscoe, J. A. Slavin, and R. P. Lepping (1986), Major Flattening of the Distant Geomagnetic Tail, *J. Geophys. Res.*, 91(A4), 4223–4237.
- Sibeck, D. G., R. E. Lopez, and E. C. Roelof (1991), Solar Wind Control of the Magnetopause Shape, Location, and Motion, *J. Geophys. Res.*, 96(A4), 5489–5495.
- Siscoe, G., and N. Crooker (1974), A Theoretical Relation between Dst and the Solar Wind Merging Electric Field, *Geophys. Res. Lett.*, 1(1), 17–19.
- Siscoe, G. L., G. M. Erickson, B. U. Ö. Sonnerup, N. C. Maynard, J. A. Schoendorf, K. D. Siebert, D. R. Weimer, W. W. White, and G. R. Wilson (2002a), Hill model of transpolar potential saturation: Comparisons with MHD simulations, *J. Geophys. Res.*, 107(A6), 1075, doi:10.1029/2001JA000109.
- Siscoe, G. L., N. U. Crooker, and K. D. Siebert (2002b), Transpolar potential saturation: Roles of region 1 current system and solar wind ram pressure, *J. Geophys. Res.*, 107(A10), 1321, doi:10.1029/2001JA009176.
- Siscoe, G., J. Raeder, and A. J. Ridley (2004), Transpolar potential saturation models compared, *J. Geophys. Res.*, 109, A09203, doi:10.1029/2003JA010318.
- Smith, C. W., B. J. Vasquez, and K. Hamilton (2006), Interplanetary magnetic fluctuation anisotropy in the inertial range, *J. Geophys. Res.*, 111, A09111, doi:10.1029/2006JA011651.
- Sonnerup, B. U. Ö. (1979), Magnetic field reconnection, in *Solar System Plasma Physics*. Volume III, L. T. Lanzerotti, C. F. Kennel and E. N. Parker (eds.) pg. 45, North-Holland Publishing, New York.
- Spreiter, J. R., A. L. Summers, and A. Y. Alksne (1966a), Hydromagnetic flow around the magnetosphere, *Planet. Space Sci.*, 14, No. 3, 223–253.
- Spreiter, J. R., A. Y. Alksne, and B. Abraham-Shrauner (1966b), Theoretical proton velocity distributions in the flow around the magnetosphere, *Planet. Space Sci.*, 14, No. 11, 1207–1220.
- Suvorova, A., A. Dmitriev, J.-K. Chao, M. Thomsen, and Y.-H. Yang (2005), Necessary conditions for geosynchronous magnetopause crossings, *J. Geophys. Res.*, 110, A01206, doi:10.1029/2003JA010079.

- Swisdak, M., and J. F. Drake (2007), Orientation of the reconnection X-line, *Geophys. Res. Lett.*, 34, L11106, doi:10.1029/2007GL029815.
- Taylor, M. G. G. T., et al. (2008), The plasma sheet and boundary layers under northward IMF: A multi-point and multi-instrument perspective, *Adv. Space Res.*, in press.
- Thomsen, M. F., J. T. Gosling, S. J. Bame, and M. M. Mellott (1985), Ion and Electron Heating at Collisionless Shocks Near the Critical Mach Number, *J. Geophys. Res.*, 90(A1), 137–148.
- Tidman, D. A., and N. A. Krall (1971), *Shock Waves in Collisionless Plasmas*, Sect. 1.6, Wiley, New York.
- Vasyliunas, V. M. (1984), Steady state aspects of magnetic field line merging, in *Magnetic Reconnection in Space and Laboratory Plasmas*, E. W. Hones (ed.), pg. 25, American Geophysical Union, Washington.
- Vasyliunas, V. M. (2004), Comparative magnetospheres: Lessons for Earth, *Adv. Space Res.*, 33(11), 2113–2120.
- Walker, A. D. M. (1981), The Kelvin-Helmholtz instability in the low-latitude boundary layer, *Planet. Space Sci.*, 29(11), 19.
- Walters, G. K. (1964), Effect of oblique interplanetary magnetic field on shape and behavior of the magnetosphere, *J. Geophys. Res.*, 69, 1769.
- Weimer, D. R., L. A. Reinleitner, J. R. Kan, L. Zhu, and S. -I. Akasofu (1990), Saturation of the Auroral Electrojet Current and the Polar Cap Potential, *J. Geophys. Res.*, 95(A11), 18,981–18,987.
- Winglee, R. M., D. Chua, M. Brittnacher, G. K. Parks, and G. Lu (2002), Global impact of ionospheric outflows on the dynamics of the magnetosphere and cross-polar cap potential, *J. Geophys. Res.*, 107(A9), 1237, doi:10.1029/2001JA000214.
- Wilber, M., and R. M. Winglee (1995), Dawn-Dusk Asymmetries in the Low-Latitude Boundary Layer Arising from the Kelvin-Helmholtz Instability: A Particle Simulation, *J. Geophys. Res.*, 100(A2), 1883–1898.
- Wygant, J. R., R. B. Torbert, and F. S. Mozer (1983), Comparison of S3-3 Polar Cap Potential Drops with the Interplanetary Magnetic Field and Models of Magnetopause Reconnection, *J. Geophys. Res.*, 88(A7), 5727–5735.
- Yamauchi, M., H. Nilsson, L. Eliasson, O. Norberg, M. Boehm, J. H. Clemmons, R. P. Lepping, L. Blomberg, S.-I. Ohtani, T. Yamamoto, T. Mukai, T. Terasawa, and S. Kokubun (1996), Dynamic response of the cusp morphology to the solar wind: A case study during passage of the solar wind plasma cloud on February 21, 1994, *J. Geophys. Res.*, 101, 24675–24687.
- Zhuang, H. C., C. T. Russell, and R. J. Walker (1981), The influence of the interplanetary magnetic field and thermal pressure on the position and shape of the magnetopause, *J. Geophys. Res.*, 86(1), 10009–10021.
- Zwan, B. J., and R. A. Wolf (1976), Depletion of Solar Wind Plasma Near a Planetary Boundary, *J. Geophys. Res.*, 81(10), 1636–1648.

Low Mach number solar wind effect	Observational evidence	Physical understanding	Section
Low- $\beta$ magnetosheath	Confirmed	Yes	3.2
Flow enhancements in magnetosheath	Confirmed	Yes	3.3
Asymmetric magnetosheath flows	To confirm	Yes	3.3
Asymmetric magnetopause	To confirm	Yes	3.4
Faster onset of the KH instability	Suggestive	Poor	3.5
Spiral auroral features	To confirm	Poor	3.5
Changes in dayside reconnection rate	To confirm	Yes	3.6
“Density” effect on reconnection rate	Suggestive	Yes	3.6
Cross polar cap potential saturation	Confirmed	Poor	3.7
Global sawtooth oscillations	Suggestive	Poor	3.8
Alfvén wings	To confirm	Yes	3.9
Enhanced plasmasphere effect	To confirm	Yes	3.9
Changes to plasma depletion layer	To confirm	Yes	3.9
Sunward displacement of the cusps	To confirm	Yes	3.9
Ti/Te ratio lower than 6-7	To confirm	Yes	3.9
Lower bow shock reflection/acceleration	To confirm	Poor	3.9
Lower turbulence in magnetosheath	To confirm	Poor	3.9

**Table 1.** List of the low Mach number solar wind effects at the Earth’s magnetosphere and the current status of observational evidence and physical understanding (from the present MHD simulations) for them.

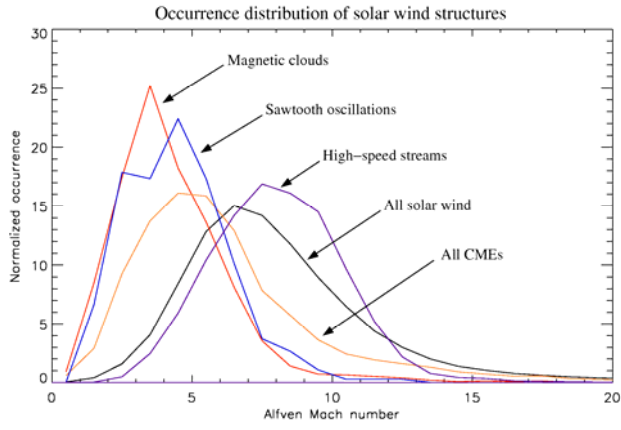


**Figure 1.** Normalized occurrence distribution (in %) of solar wind Mach numbers from the OMNI dataset, for various solar wind structures: (1) all solar wind conditions, (2) coronal mass ejections (CME), (3) magnetic clouds (MC), (4) high-speed streams (HSS) and (5) sawtooth oscillation (SO) intervals. These intervals were taken from various sources (see section 2). The histogram sampling is made using a unit Alfvén Mach number bin size.

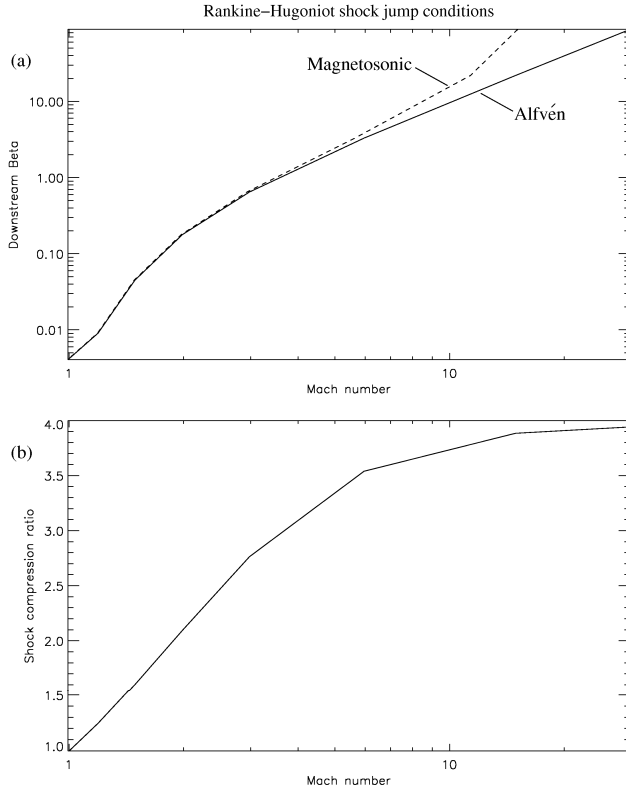


**Figure 2.** (a) Downstream magnetosheath thermal  $\beta$  values as a function of Alfvén (solid) and Magnetosonic (dashed) Mach numbers, as calculated from Rankine-Hugoniot MHD jump conditions. We used a solar wind speed of 650 km/s, a density of  $1 \text{ cm}^{-3}$ ,  $\gamma = 5/3$  and ion and electron temperatures of 50000 K. The magnetic field strength was varied from 1 to 30 nT. (b) The magnetic field compression ratio at a perpendicular shock as a function of the Alfvén Mach number, for the same set of upstream conditions.

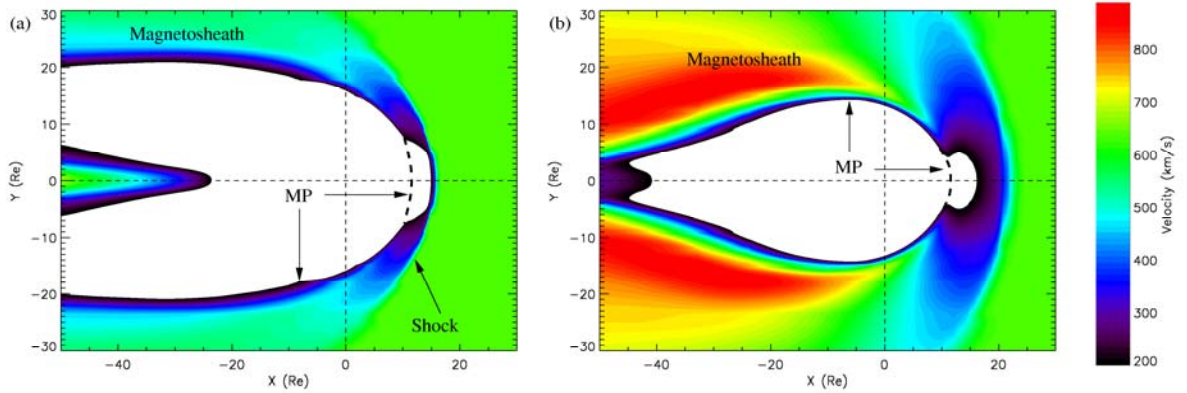


**Figure 3.** Equatorial two-dimensional (2D) cuts of the plasma speed from two global MHD simulations with solar wind Alfvén Mach numbers (a)  $M_A = 14.90$  and (b)  $M_A = 1.99$ . For these runs the solar wind magnetic field is purely northward, respectively of  $B_Z = 2$  and 15 nT, with solar wind plasma density  $N = 1 \text{ cm}^{-3}$ , speed  $V = V_x = -650 \text{ km/s}$ , and temperature  $T = 50000 \text{ K}$ . This temperature is used throughout the paper since CMEs typically have such low temperatures. Both figures present the flow speed according to the color palette given in the right hand side.

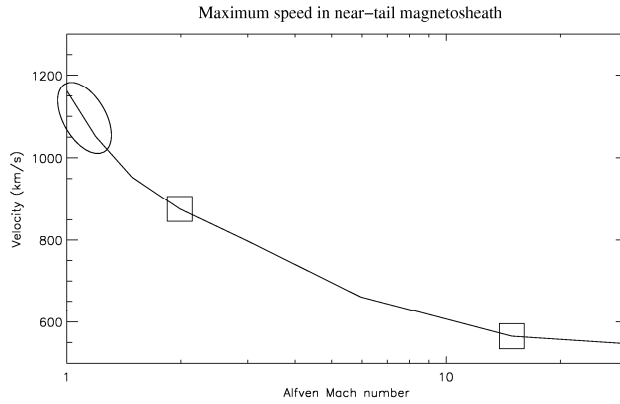


**Figure 4.** Maximum equatorial speed in the magnetosheath in the region comprised in the range  $X = [-10, -50] R_E$  and  $Y = [-10, -30] R_E$  (refer to Figure 3 for context), as a function of Mach number from several MHD runs. The plasma parameters are the same as for Figure 3, except that the northward magnetic field strength is varied between 1 and 30 nT (eight values). The two squares show the regimes from which Figures 3a and 3b were taken. The ellipse encircles the results for the two lowest Mach number values when the bow shock intersects the upper and lower boundaries of the simulations. This sometimes results in wave reflection effects, but we made additional runs to ensure that those flow results are not affected.

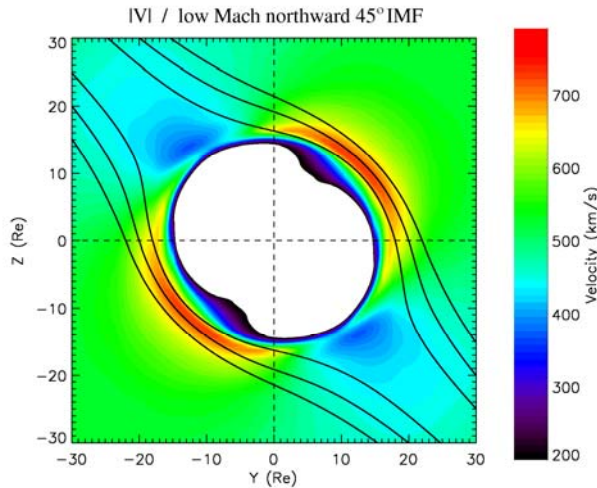


**Figure 5.** Y-Z 2D cut of the plasma flow speed in the  $X = -5 R_E$  plane for the same low Mach number solar wind parameters as in Figure 3b (i.e.,  $M_A = 1.99$ ). For this figure, however, the IMF direction was set with a clock angle of  $45^\circ$  from the pure northward IMF, in order to illustrate the dependence of the enhanced flow location on the IMF orientation. Sample field lines in the magnetosheath illustrate this orientation.

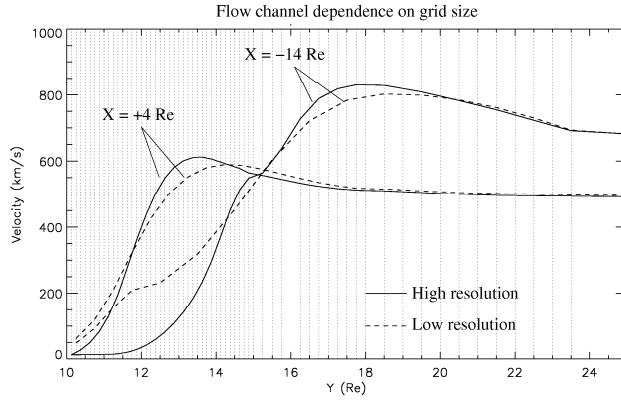


**Figure 6.** 1D cuts of the plasma flow speed from the tail and into the magnetosheath at dusk, at two distances of  $X = -4$  and  $-14 R_E$ , and as a function of the MHD simulation grid resolution for the northward IMF run with  $M_A = 1.99$  (see Figure 3b). The profiles of the flow speed are shown as solid lines for the highest resolution and dashed lines for the lower resolution (about twice lower). The highest resolution in the cut plane is shown with faint dotted lines in the Figure for context.

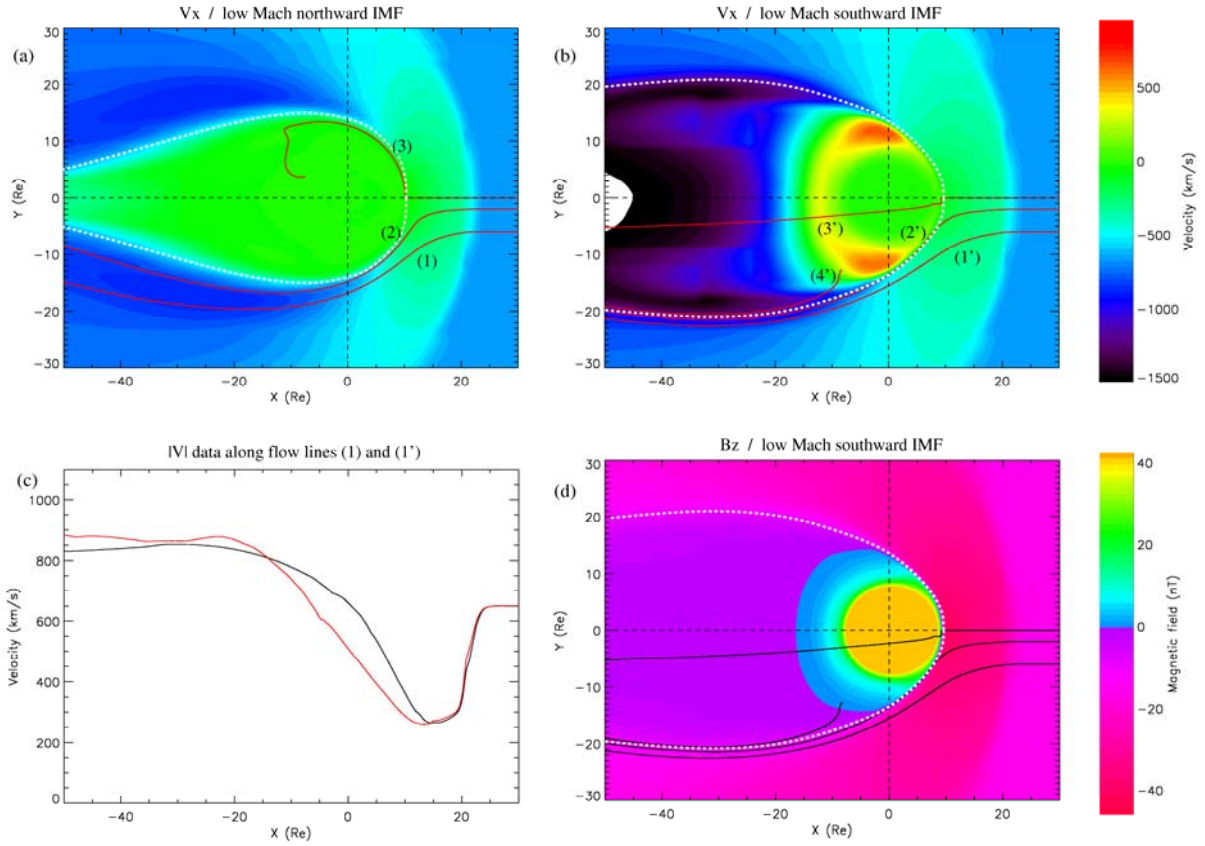


**Figure 7.** Illustration of the dependence of magnetosheath properties on IMF orientation. Figure 7a is the same as Figure 3b, i.e., it is for a low  $M_A$  under pure northward IMF, except that it shows the X component of the plasma velocity with a different color palette (which changes the dynamic range as compared to Figure 3), and that three plasma flow streamlines starting at  $X = 33 R_E$  and  $Y = 0, -2$  and  $-6 R_E$  are over-plotted. Figures 7b and 7d are for the same solar wind conditions, except that the IMF is oriented purely southward, instead of northward. Figure 7b shows the X component of the plasma velocity while Figure 7d shows the  $B_z$  component, both in the equatorial plane. Three flow streamlines with the same starting point as for Figure 7a are shown, but an additional streamline (4') is added to highlight the magnetopause location (see text for details). Figure 7c shows the plasma flow speed along the flow streamlines labeled (1: black line) and (1': red line) in the other plots. It shows that enhanced flows of the same order of magnitude are found adjacent to the magnetopause in both the northward and southward IMF cases, under low Mach number conditions.



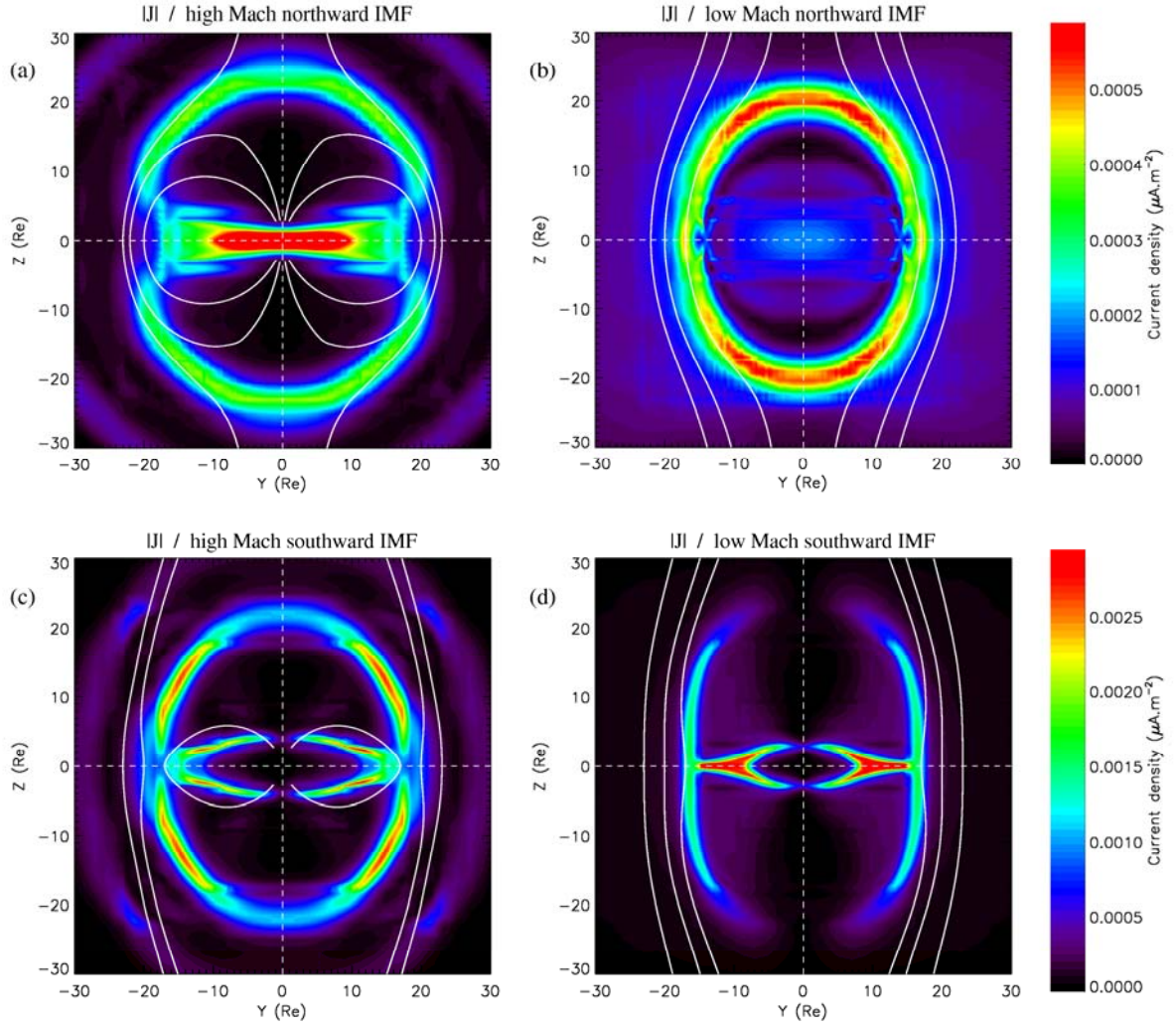


**Figure 8.** 2D cuts of the current magnitude for high ((a) and (c) with  $M_A = 14.90$ ) and low ((b) and (d) with  $M_A = 1.99$ ) Mach numbers and for northward ((a) and (b) at  $X = -15 R_E$ ) and southward ((c) and (d) at  $X = -5 R_E$ ) IMF orientations. Sample field lines are over-plotted. These and the current magnitude are used here to highlight the magnetopause position, which appears elongated in the case of low Mach numbers. It appears that the magnetopause is most elongated, even already at  $X = -5 R_E$ , in the case of southward IMF and low Mach number.

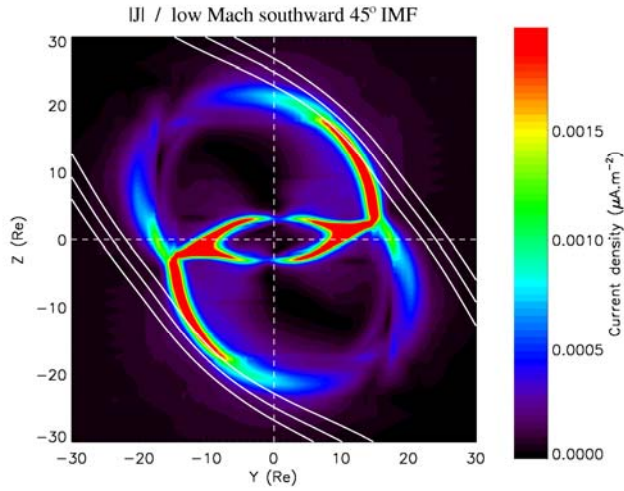


**Figure 9.** Y-Z 2D cut of the current magnitude from an MHD simulation with low  $M_A = 1.99$  at  $X = -5 R_E$  in the case of an IMF oriented at  $45^\circ$  from the pure southward direction. Sample field lines are over-plotted for context. It shows that the magnetopause elongation follows the IMF orientation.

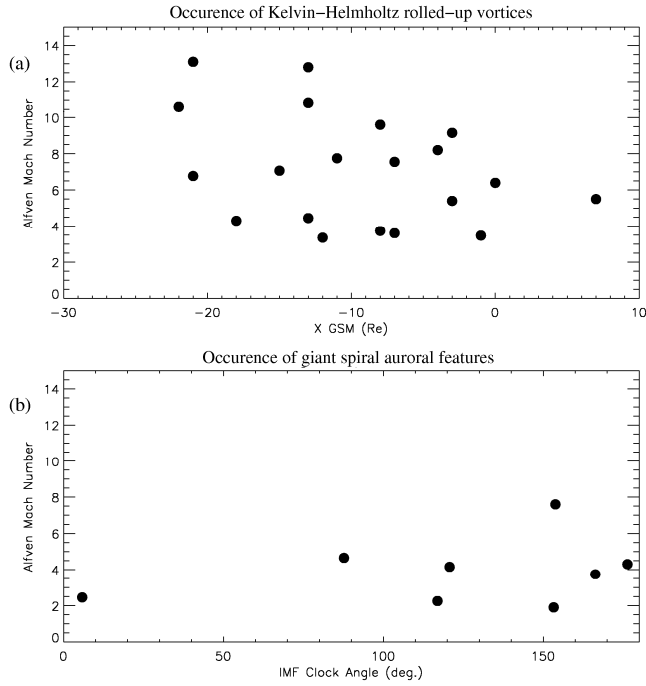


**Figure 10.** Prevailing solar wind Alfvén Mach number as a function of: (a) the downtail spacecraft distance at the time of observation of rolled-up Kelvin-Helmholtz vortices (from the list of Hasegawa et al., [2006]); (b) the average IMF clock angle during intervals of giant auroral spiral features found during intense geomagnetic storms ( $D_{ST} < -250$  nT). See section 3.5 for details.

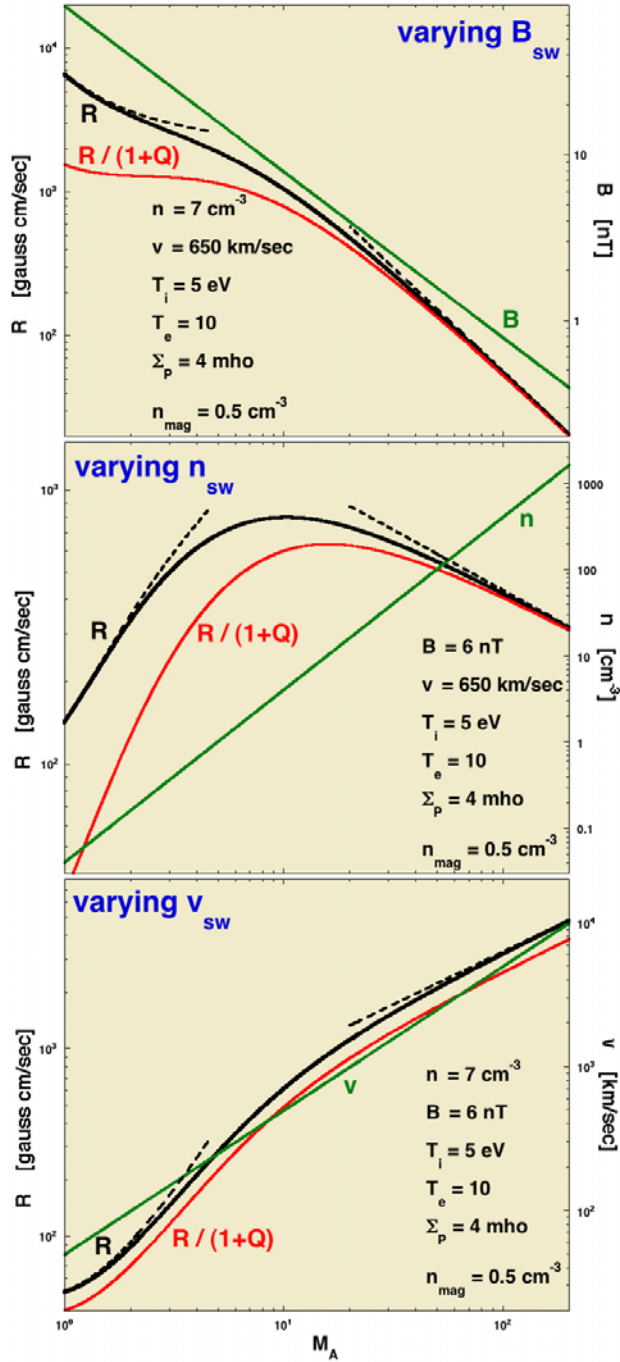


**Figure 11.** Reconnection rate as a function of solar wind Mach number, as obtained from Eq. (2), and resulting from varying separately the solar wind (a) magnetic field, (b) density, and (c) speed. The asymptotic curves are shown as dashed lines. The varying solar wind parameters are shown with green curves and the other parameter values used for each panel are given in the figures. The reconnection rates scaled by the effect of the saturation parameter  $Q$  (see section 3.7) are displayed with red curves. A “density” effect can be observed in panel (b) in the low Mach number regime (see text for further details). The reader should note that this is a parametric representation of Eq. (2); the ranges of variation (at high Mach numbers in particular) are not necessarily realistic.

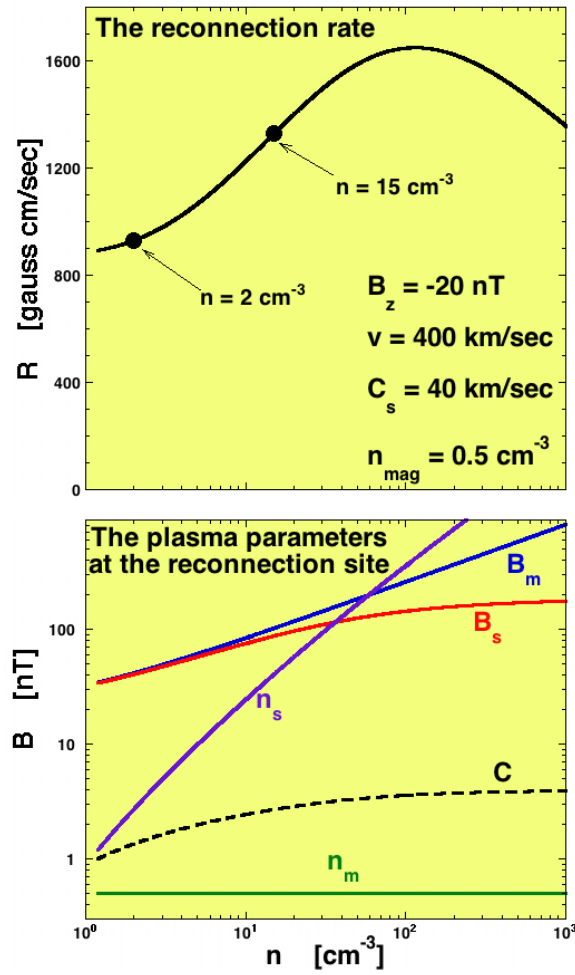


**Figure 12.** (a) Reconnection rate as a function of solar wind density using Eq. (1), as for Figure 11.  $C_s$  is the value of the sound speed. (b) Values of the plasma parameters near the reconnection site obtained from the same equation and using a constant low magnetospheric density ( $n_m = 0.5 \text{ cm}^{-3}$ ).  $B_m$  = magnetospheric magnetic field magnitude;  $B_s$  = magnetosheath magnetic field magnitude;  $n_s$  = magnetosheath density;  $C$  = perpendicular shock compression ratio.

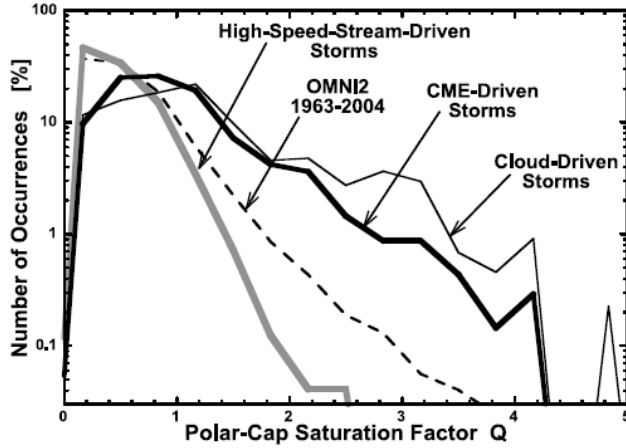


**Figure 13.** Occurrence statistics of the CPCP saturation, as expected from the Q factor of the Hill-Siscoe model, for different sorts of solar wind structures (cf. section 2), and obtained using OMNI data over the years 1989 - 2003. See text for further details. Figure from *Borovsky and Denton* [2006a].

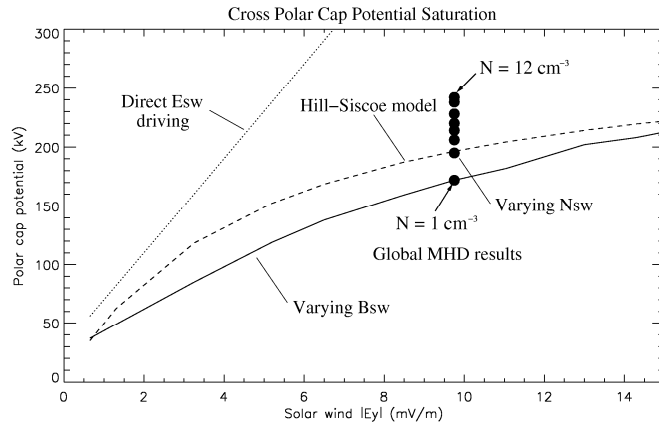


**Figure 14.** Cross polar cap potential saturation results from global MHD simulations. The solid line shows results from varying the magnitude of the southward magnetic field, with a solar wind density of  $1 \text{ cm}^{-3}$ , a velocity of  $650 \text{ km/s}$  and an ionospheric conductance of  $4 \text{ S}$  (i.e., as in most runs throughout this paper). The solid points show results from varying the solar wind density between  $1$  and  $15 \text{ cm}^{-3}$ , using a constant southward magnetic field of  $B_z = -15 \text{ nT}$ , i.e., corresponding to a constant solar wind electric field. The dashed line shows the estimation from the Hill-Siscoe model [Siscoe *et al.*, 2002a] using the same values as for the solid line. The dotted line shows the expected potential from a simple model assuming direct solar wind driving, i.e., with no saturation. See text for details.

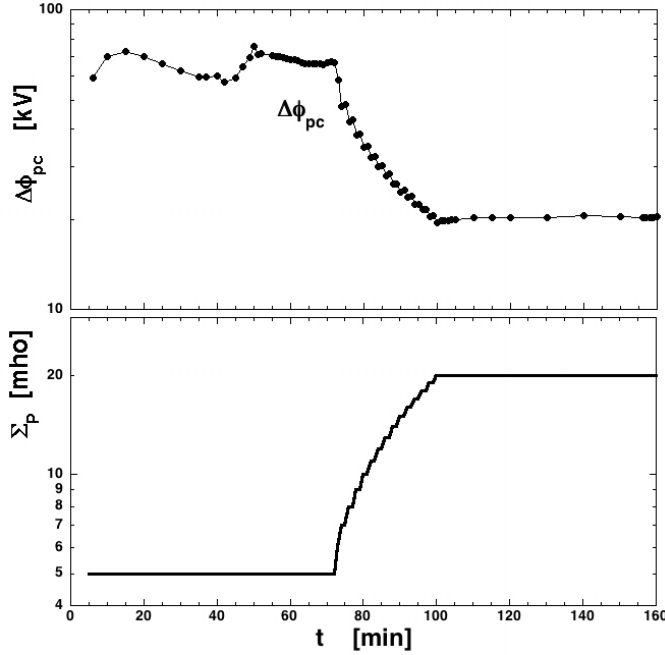


**Figure 15.** Variations of the (a) CPCP ( $\Delta\Phi_{pc}$ ) and (b) ionospheric conductance ( $\Sigma_p$ ) during the special global MHD run with high resolution and a resistive “spot” at the dayside magnetopause. See text for details.

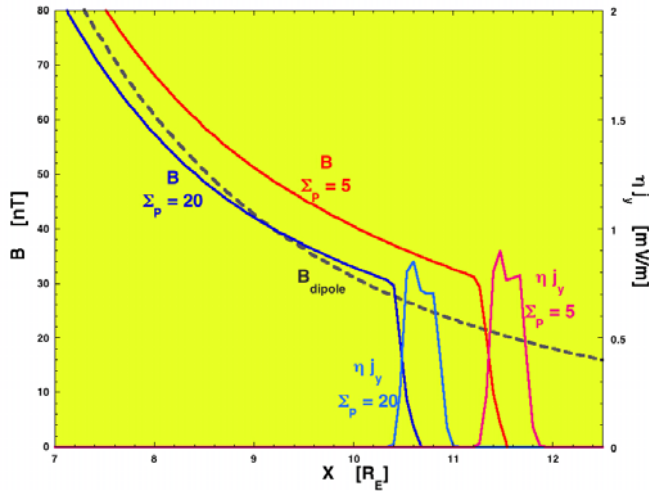


**Figure 16.** Profiles of the magnetic field magnitude in the dayside magnetosphere along the Sun-Earth line, for the special MHD run of Figure 15 at times of low (red line) and high ionospheric conductivities (blue line). The black dashed curve corresponds to the regular dipole magnetic field strength. The resistive electric field (axis to the right), which corresponds to the reconnection rate at the dayside magnetopause, is also plotted for those two cases (light blue and magenta). While the magnetic field in the magnetosphere is lower for a high conductance, owing to the feedback of increased region 1 current, the magnetic field magnitude near the reconnection region and thus the reconnection rate are essentially not altered.



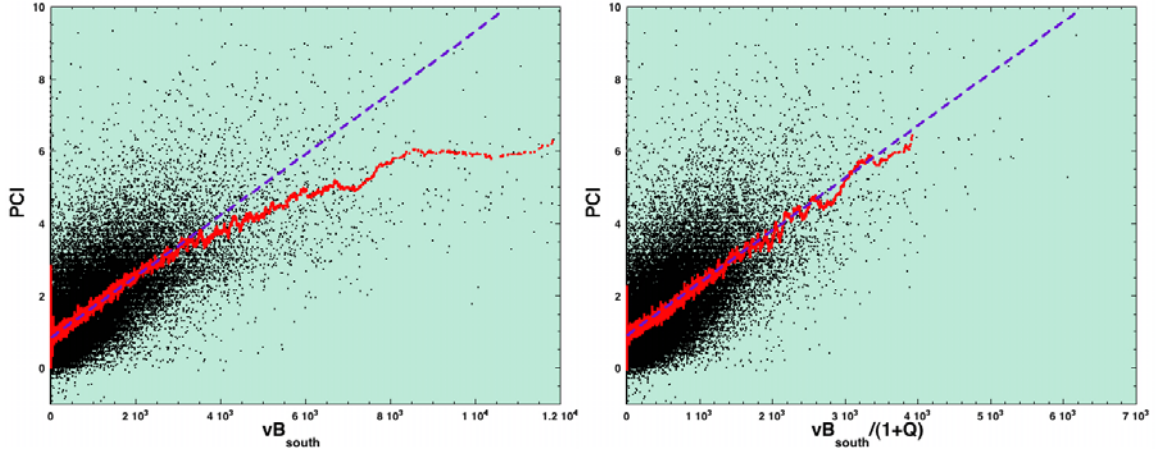


**Figure 17.** Scatter plot of the value of the polar cap index (PCI) as a function of solar wind driving ( $vB_{\text{south}}$ ) (a) without correction and (b) with correction using the  $Q$  factor as introduced in the text and in Eq. (7). The red curves show a 100-point running average along the  $vB_{\text{south}}$  parameter. The right-hand plot shows that the  $Q$  factor correction is able to account for the saturation in the high driving regime on average.

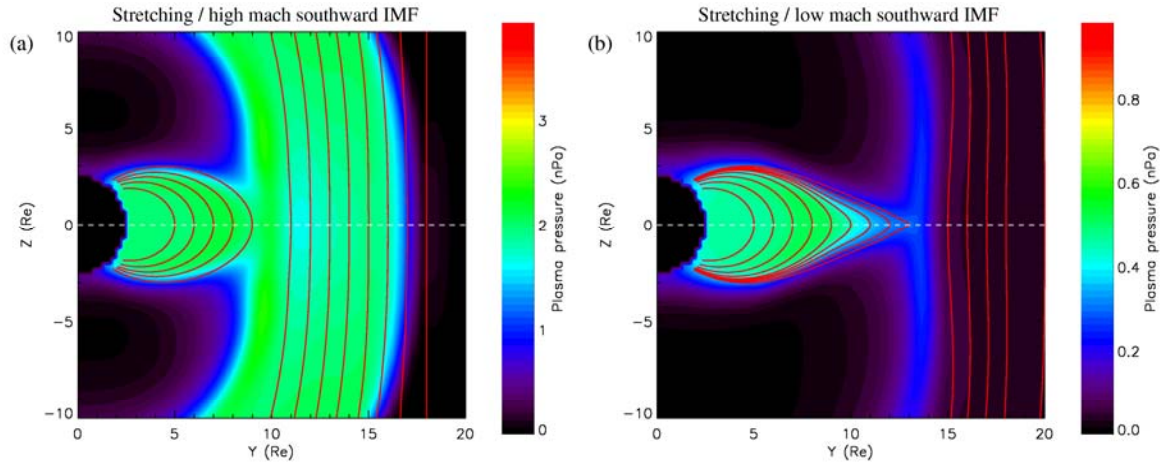


**Figure 18.** Y-Z 2D cuts of the plasma pressure for (a) high  $M_A = 6.88$  and (b) low  $M_A = 1.99$  at  $X = 0 R_E$  (dawn-dusk terminator) from MHD simulations with an IMF oriented purely southward and during strong driving with  $B_Z = -15$  nT and  $|V| = 650$  km/s. Sample field lines in that plane are over-plotted in red for context. These show that during strong driving a substantial stretching of the magnetic field occurs primarily if the Mach number is low.

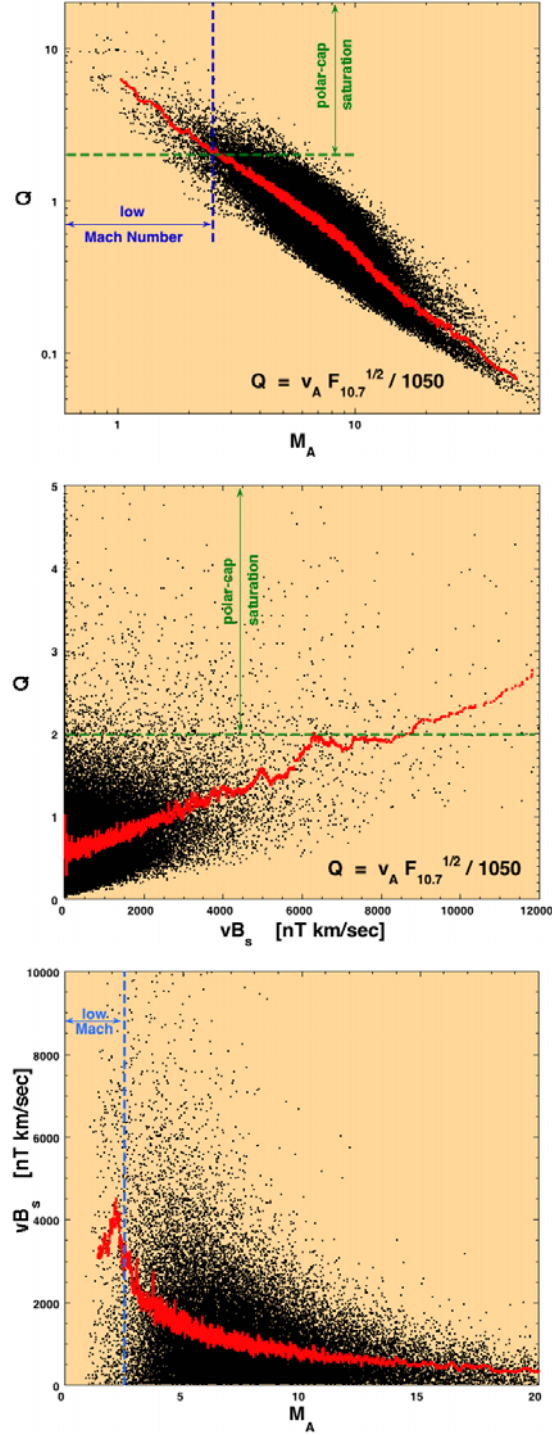


**Figure 19.** Scatter plots of one-hour averaged solar wind data from OMNI (over the years 1989 – 2003): (a) Q factor as a function of Mach number, (b) Q factor as a function of solar wind electric field, and (c) solar wind electric field as a function of Mach number. The red curves show a 100-point running average along the abscise parameter. These show that large driving solar wind electric field, low Mach number solar wind and CPCP saturation all tend to occur at the same time at Earth (i.e., typically during CME-driven storms). See text for details.